TIGHT GAS SANDS LIBRARY - WGSP
UCRL - 50036 - 80 - 1

DB-374

UCRL-50036-80-1

LLNL gas stimulation program quarterly progress report January through March 1980

M. E. Hanson, G. D. Anderson,
R. J. Shaffer, D. F. Towse,
W. Lin, M. P. Cleary, D. R. Peterson,
S. K. Wong, and B. C. Haimson

May 5, 1980

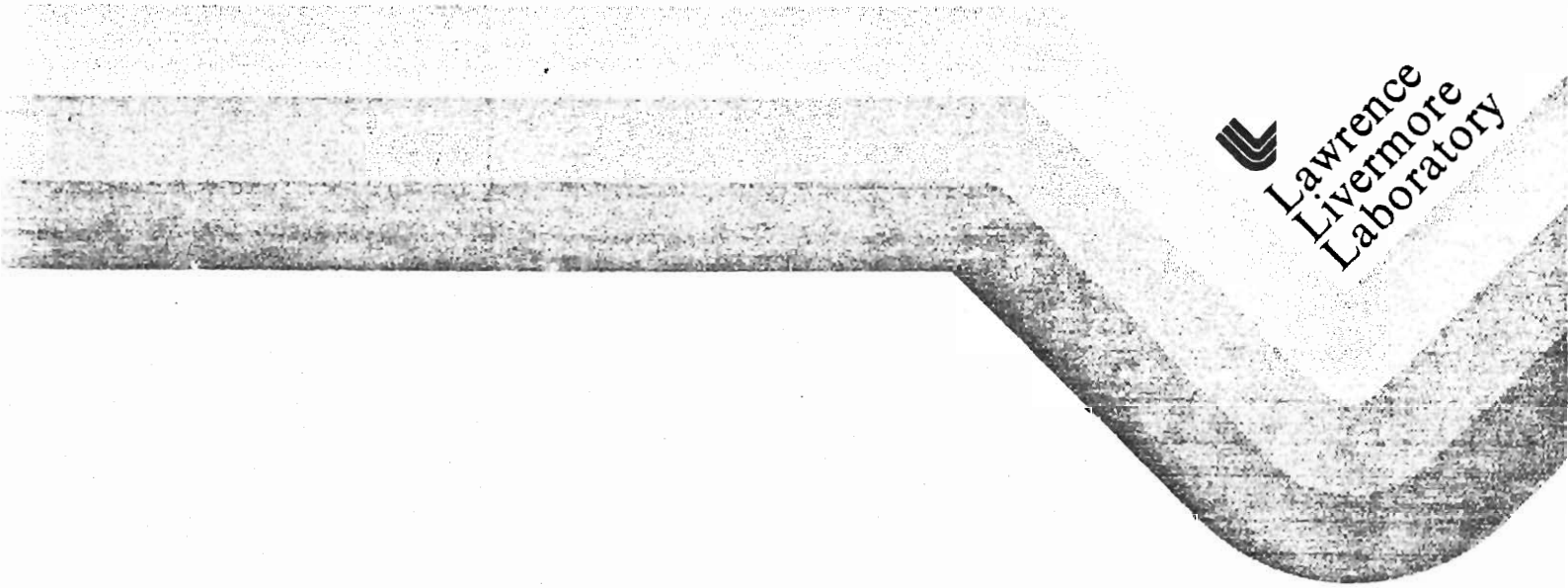

This report was prepared as an account of work sponsored by the United States Government. Neither the United States nor the United States Department of Energy, nor any of their employees, nor any of their contractors, subcontractors, or their employees, makes any warranty, express or implied, or assumes any legal liability or responsibility for the accuracy, completeness or usefulness of any information, apparatus, product or process disclosed, or represents that its use would not infringe privately owned rights.

Reference to a company or product name does not imply approval or recommendation of the product by the University of California or the U.S. Department of Energy to the exclusion of others that may be suitable.

Work performed under the auspices of the U.S. Department of Energy by the Lawrence Livermore Laboratory under Contract W-7405-Eng-48.

UCRL-50036-80-1
Distribution Category UC-92a

LLNL gas stimulation program quarterly progress report January through March 1980

M. E. Hanson, G. D. Anderson,
R. J. Shaffer, D. F. Towse,
W. Lin, M. P. Cleary*, D. R. Peterson*,
S. K. Wong,* and B. C. Haimson**

Manuscript date: May 5, 1980

*Affiliated with Massachusetts Institute of Technology

**Affiliated with the University of Wisconsin

CER CORPORATION
LIBRARY

LAWRENCE LIVERMORE LABORATORY
University of California • Livermore, California • 94550

Available from: National Technical Information Service • U.S. Department of Commerce
5285 Port Royal Road • Springfield, VA 22161 • $6.00 per copy • (Microfiche $3.50)

PREFACE

Although U.S. gas resources remain large, proven reserves have declined to 230 trillion feet, and the current reserves/production ratio is 10 to 1.

It is estimated that tight (i.e., low permeability) western gas reservoirs and eastern Devonian gas shales contain large quantities of natural gas, but because of the low permeability, these resources have been difficult to recover. Some gas has been produced, but industry needs more economical recovery techniques. The region around the production wells must be stimulated in some manner to induce a more rapid flow into the well bore. The stimulation process involves creating channels or cracks out into the reservoir from the well bore. This can be done by detonating high explosives or nuclear explosives in the well bore or by hydraulically fracturing the formation.

Currently, the most promising techniques for stimulating low-permeability gas reservoirs are hydraulic fracturing and massive hydraulic fracturing (MHF). Hydraulic fracturing involves pumping fluids under high pressure down the well bore and out into the reservoir. The hydraulic action fractures the rock around the well bore, and proppants in the fracturing fluids hold the cracks open. The fractures provide large drainage faces for the gas and channel it into the well bore. Hydraulic fracturing has been routinely used in oilwell completion and cleanup for many years. MHF differs from hydraulic fracturing in that larger amounts of fluid and proppant are pumped down the well to create and prop fractures at much greater distances.

The application of MHF techniques to tight western gas formations has given variable and sometimes disappointing results. The best efforts of a CER-led industry/government consortium to stimulate the Piceance Basin near Rio Blanco, Colorado, were not successful. On the other hand, Amoco has used MHF techniques in the Wattenburg Field near Denver with a high degree of success. Significant differences in the reservoirs themselves apparently account for the differences in success.

The Devonian shales present similar problems. It is believed that production from these gas shales results from the connection of the wells to the existing fracture patterns. Hence, to recover this gas, we must locate the producing zones, locate the natural fractures near the well bore, and fracture from the well bore to the existing fractures.

The Lawrence Livermore National Laboratory (LLNL) has embarked on a research program to help develop tight gas reservoirs in the United States. We are trying to obtain a more detailed understanding of the stimulation processes, including how the formation properties interact with and affect these processes. The problem is to determine how to connect the maximum amount of productive reservoir rock to the well bore through a highly permeable fracture system.

There are several questions that we would like to be able to answer in advance about the tight Rocky Mountain formations. Can we identify particular sections where the fractures may be expected to be preferentially confined to the productive sands, so that a maximum volume of reservoir can be stimulated? What is the geometry (length, width, and number) of the fractures? What is the nature of the treatment (fluid composition, volumes, pumping rates, perforation intervals) which, when applied to a formation with certain properties, will result in optimum and economical recovery? What are some of the important geophysical measurements and experiments that can aid in this endeavor? What data and experiences exist that are relevant? Most of the western reservoirs contain a high degree of water saturation, which can significantly reduce the already low permeability of these reservoirs: is it possible to use existing logging techniques supplemented by new geophysical measurements to ascertain the *in situ* water saturation?

Devonian shales present many of the same challenges as the tight Rocky Mountain formations. There are, however, some special problems. Logging techniques for these shales are just being developed, and we have not yet acquired the ability to locate the fractures that do not intersect the well bore. The effect of hydraulic fracturing on Devonian shales is also not well understood. Water, one of the standard hydraulic fracturing fluids, can cause significant formation damage; organic and cryogenic fluids are expensive; high-explosive fracturing makes well clean-out and completion costly and uncertain; and, as we have shown previously, the diameter of permeability enhancement is small.

Our program is primarily investigative, and we are constructing and applying theoretical models and performing laboratory experiments to develop an understanding of the gas stimulation process. These tasks

are complementary, and parallel development is necessary. Another facet of the program is geophysical measurement (logging) in the environments where these stimulation processes are applied. Close association with the DOE-supported field programs provides the interaction and direction necessary to the program.

The LLNL program can be broken into eight task areas: (1) theoretical modeling of the hydraulic process, (2) laboratory hydraulic fracturing experiments, (3) log tool development and analysis of log data, (4) cataloging and evaluation of pertinent geological and geophysical reservoir data, (5) measurement of pertinent reservoir properties, (6) reservoir analysis, (7) evaluation of other stimulation techniques, and (8) environmental reports in support of DOE field programs.

LLNL gas stimulation program quarterly progress report January through March 1980

ABSTRACT

This report summarizes the research and accomplishments of the LLNL Gas Stimulation Program during the second quarter of FY 1980. We have continued to analyze the effects of dynamics and fractures on hydraulic fracture propagation near interfaces. We have also begun some analysis of the propagation of penny-shaped cracks including an averaged flow description in the cracks. Poiseuille flow descriptions of Newtonian fluids were used to model the fluid flow and pressure distribution in the crack. Frictional effects and measurements were emphasized in the laboratory experiments. These results show that variation in friction along an interface can result in abrupt steps in the fracture path. We have also completed a laboratory study of the effects of fluid viscosity on fracture orientation under various stress states. Results from these experiments indicate that the fluid viscosity does not significantly affect the fracture orientation; however, increases in fluid viscosity result in higher breakdown pressures. We have continued to study the relation between natural fractures and structural geology in the Piceance Basin.

THEORETICAL ANALYSES

EFFECTS OF FRICTION AND DYNAMICS

The equations of motion for an elastic continuum can be written as

$$\frac{\partial \sigma_x}{\partial x} + \frac{\partial \tau_{xy}}{\partial y} = \rho \frac{\partial^2 u}{\partial t^2}$$

and

$$\frac{\partial \sigma_y}{\partial y} + \frac{\partial \tau_{xy}}{\partial x} = \rho \frac{\partial^2 v}{\partial t^2} \tag{1}$$

where t is time, ρ is density, τ_{xy} is the shear stress, and σ_x and σ_y are normal stresses and u and v are displacements in the x and y directions, respectively. The stresses are related to the strains with the constitutive relations:

$$\begin{Bmatrix} \sigma_x \\ \sigma_y \\ \tau_{xy} \end{Bmatrix} = \begin{bmatrix} 2\mu+\lambda & \lambda & 0 \\ \lambda & 2\mu+\lambda & 0 \\ 0 & 0 & \mu \end{bmatrix} \begin{Bmatrix} \frac{\partial u}{\partial x} \\ \frac{\partial v}{\partial y} \\ \frac{\partial u}{\partial y} + \frac{\partial v}{\partial x} \end{Bmatrix} \tag{2}$$

where λ and μ are the Lamé constants. Then a unique problem is specified by supplying the proper initial and boundary conditions.

We discretized Eq. (1) in space with bilinear forms.[1] When the displacements are time independent, this discretization leads to a stiffness matrix that relates point forces to point displacements. We relax this matrix with an iteration scheme that is a variation of the incomplete Cholesky-conjugate gradient method by Kershaw.[2] We also use this iteration scheme to solve the mass matrix that arises in time dependent problems.

Equilibrium Crack Growth Near a Frictional Interface

Some reservoir characteristics which can exert control on fracture geometry include changes in material properties across a material interface and frictional slip along existing fractures and poorly bonded bedding planes. We have previously reported results of analyses on some of the effects on fracturing near material interfaces.[3,4] In shallow reservoirs, frictional slip along an existing fracture or along poorly bonded bedding planes can effectively arrest propagation. Variations in the frictional coefficient can modify the path of the fracture. For example, the fracture geometry may display a sharp step due to frictional variation along a discontinuity.

We have been applying two-dimensional equilibrium models to study some aspects of fracture propagation as a fracture approaches a frictional discontinuity at right angles to the axis (direction of propagation) of the fracture. The equilibrium equations used to describe the elastic continuum are:

$$\frac{\partial \sigma_x}{\partial x} + \frac{\partial \tau_{xy}}{\partial y} = 0$$

and

$$\frac{\partial \sigma_y}{\partial y} + \frac{\partial \tau_{xy}}{\partial x} = 0 \qquad (3)$$

with the constitutive relations shown in Eq. (2) above.

The frictional stress which the interface can support is defined by

$$\tau_f = \beta \sigma_n \qquad (4)$$

where β is the coefficient of friction, and σ_n is the normal stress across the interface. The shear stress is calculated in the interface coordinate system and compared to τ_f. If the shear stress is greater than the frictional stress, slippage is allowed to occur through an iteration process until the shear stress and the frictional stress are balanced.

The effect of a frictional interface on a pressurized fracture as the crack propagates toward the interface has been analyzed. Analysis of the penetration of the interface will be the subject of future work. The geometry of the fracture and the interface used in the calculations is shown on Fig. 1. The pressure in the crack was constant and the material on both sides of the interface was identical. Poisson's ratio was equal to 0.25. The ratio of the effective pressure in the crack to Young's modulus for the material (P_c/E) was 1.5×10^{-3}. Changes in pore pressure due to leakage of fluid from the crack into the surrounding material were ignored. The fracture tip distance from the interface, δ, has been normalized with respect to the fracture length. We have completed calculations for five ratios of $\tau_f/P_c = \gamma$.

Figure 2 shows the normalized Mode I stress intensity factor as a function of δ for the values of γ = 0.033, 0.067, 0.1, 0.133, and 0.167. As expected, when the scaled distance from the crack tip to the interface is greater than 1, the effects of the frictional interface on the pressurized crack are small. The stress intensity factor is seen to increase both as the pressurized fracture approaches the interface and as the frictional coefficient becomes smaller. This is because relative motion along the interface increases in the same manner. Frictional stress along the interface changes as the fracture nears the interface. This happens when the normal stress

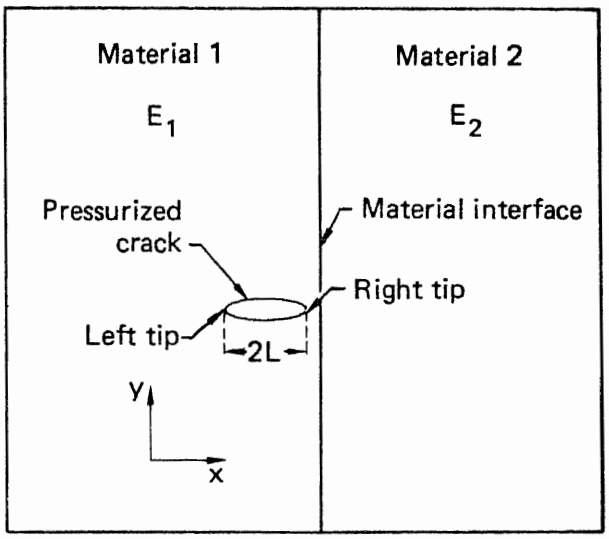

FIG. 1. Geometry of a fracture near an interface for equilibrium studies.

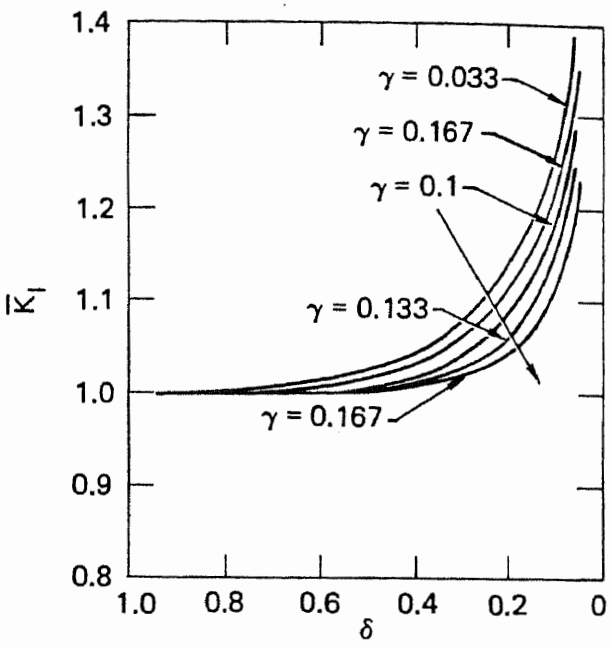

FIG. 2. Variation in Mode I stress intensity factor, as crack approaches a frictional interface, for variations in frictional stress along interface.

across the interface is reduced because the material ahead of the fracture is driven toward the tip and hence the normal stress across the interface is reduced. The largest change in the frictional stress occurs ahead of the tip where it decreases to very small values when the scaled distance is less than 0.2. Increasing the initial frictional stress along the interface delays slip until the fracture is closer to the interface; however, the stress intensity factor increases at a higher rate once slip occurs.

Dynamic Crack Growth Near a Bonded Interface

Several calculations were made with our time-dependent finite-element model in order to quantify the changes in material response due to variations in densities and elastic moduli across an interface. In the problem geometry of Fig. 3, a crack initiates at x = 0, y = 0, propagates bilaterally at half the dilatational wave speed along y = 0 for a distance "c," and stops. The densities and elastic moduli are subscripted to differentiate between their values on either side of the interface. The elapsed time from crack initiation to stopping is defined as t_b, and the strain in the z direction is set to zero. The result, shown in Figs. 4 to 6, is the time history of the vertical displacement (v) of a point just behind the final position of the right crack tip.

For all calculations the Lamé constants of material 1 were set to 0.3 Mbar (30 GPa) and the density of material 1 was 2.7 gm/cm^3. In the first set of calculations, all the Lamé constants were set equal. Three calculations were made, corresponding to three values of the density of material 2:$\rho_2 = \rho_1/9$, ρ_1, and $9\rho_1$. Hence, for the second calculation, the medium is homogeneous and the interface does not exist. The results of these three calculations are shown in Fig. 4. The displacement in the y direction has been nondimensionalized with the final half crack length, and the problem time t is nondimensionalized with the time required to break, so that $t/t_b = 1$ is the time the crack stops. For this set of calculations the crack stopped at c/L = 0.6, so that Fig. 3 is drawn to scale. As seen in Fig. 4, the variation in material response is small even for a large variation in density.

In Fig. 5, the same density variation was used, but the crack propagated up to the interface (c/L = 1.0). Here the variation in material response is larger than in the previous case, but is still small when compared to the maximum displacement. There is also a difference seen in the character of the curve for the

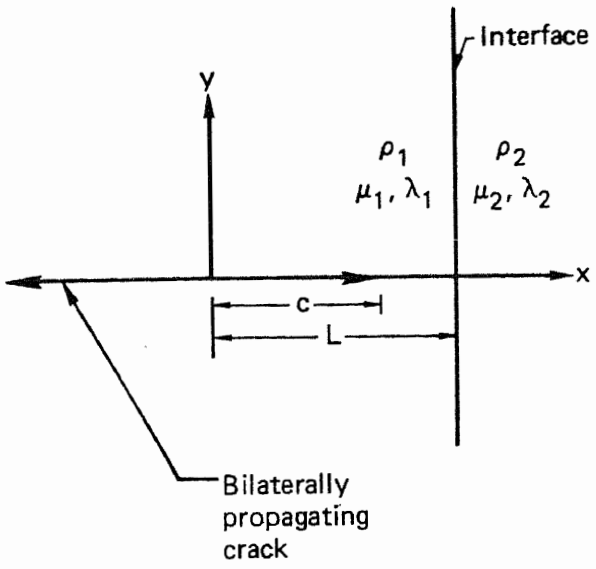

FIG. 3. Problem geometry for time-dependent crack propagation near an interface.

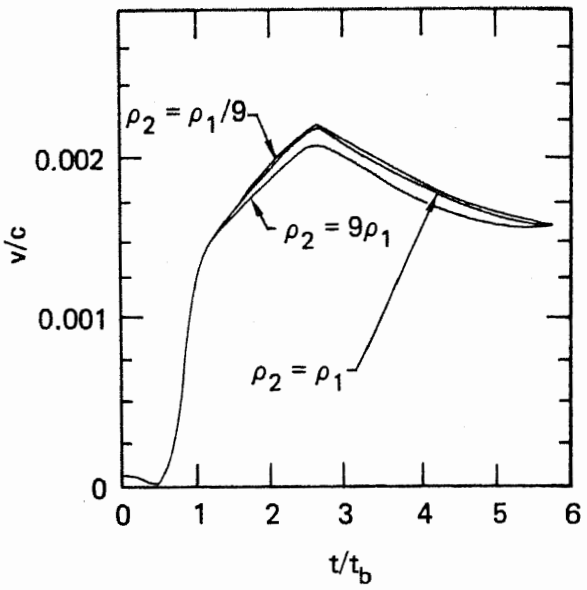

FIG. 4. Displacement perpendicular to the crack when c/L = 0.6 (the crack does not reach the interface).

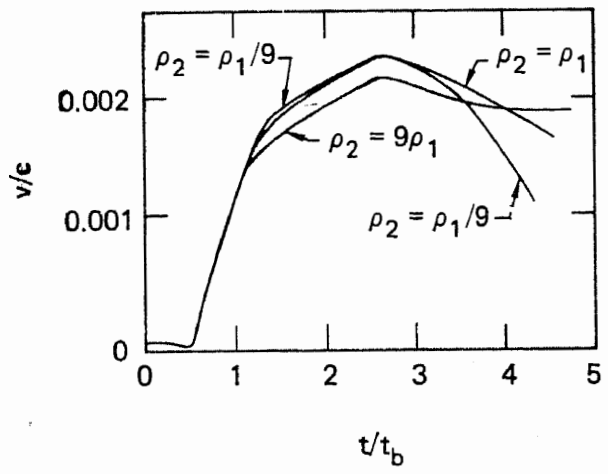

FIG. 5. Displacement perpendicular to the crack when c/L = 1.0 (the crack reaches the interface).

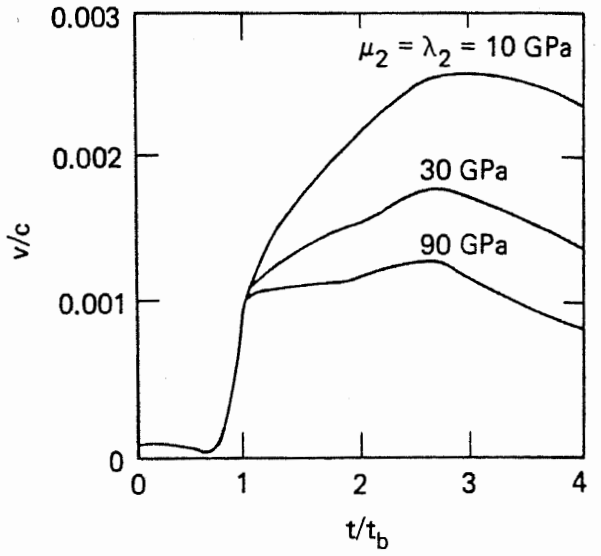

FIG. 6. Displacement perpendicular to the crack when the density is constant across the interface and c/L = 1.0.

smallest value of ρ_2 when Fig. 5 is compared to Fig. 3. This crossing over of the curves occurs long after the crack stops.

In the next set of calculations, the density was uniform ($\rho_2 = \rho_1$), and the Lamé constants for the second material were assigned the values 10 GPa, 30 GPa, and 90 GPa. The results from these three calculations are shown in Fig. 6. As in the previous case, the crack propagated to the interface (c/L = 1.0). Changing the elastic constants by a factor of three causes large changes in the material response.

We conclude that, even though wave reflection and transmission at an interface are controlled by density and elastic moduli changes across that interface, a change in elastic moduli causes a much larger variation in material response than a change in density does. It should be noted that, in Figs. 4 and 5, all the curves converge as the time becomes large; i.e., density variation is strictly a dynamic effect. This is not true of the variation in elastic constants; i.e., all the curves in Fig. 4 will approach different values as t becomes large.

FLUID FLOW AND PROPAGATION OF A CIRCULAR HYDROFRAC

Frac-Fluid Pressure Evolution

Consider a typical cross section of a penny-shaped crack with radius a, borehole radius a_b, and a fluid front at $r = a_p$ (Fig. 7). First it is possible to write an integral equation[5] relating the pressure applied to the crack surfaces $p(r,t)$ and the slope of the displacement $\partial\delta(r,t)/\partial r$:

$$\frac{1-\nu}{G}\left[p(r_o t)-\sigma_c\right]=\frac{-1}{\pi}\int_0^a \gamma(r_o,r)\,\frac{\partial\delta(r,t)}{\partial r}\,dr\,, \tag{5a}$$

where G is the shear modulus, ν is the Poisson's ratio, σ_c is the confining normal stress preexisting on the plane of the crack, and $\gamma(r_o,r)$ is the influence function given in terms of the complete elliptic integrals of the first and second kinds, K(x) and E(x), respectively, as follows:

$$\gamma(r_o,r) = \begin{cases} \frac{1}{r}K\left(\frac{r_o}{r}\right)+\frac{r}{r_o^2-r^2}E\left(\frac{r_o}{r}\right) & , \quad r_o<r \\ \\ \frac{r_o}{r_o^2-r^2}E\left(\frac{r}{r_o}\right) & , \quad r_o>r \end{cases} \tag{5b}$$

Equation (5a) is analogous to the equation in the dislocation density formulation of the two dimensional model for hydraulic fracture.[6] Experience with two-dimensional hydrofrac modeling indicates that using the opening displacement $\delta(r,t)$ instead of its slope avoids higher order differentiations which cause numerical instabilities. So we integrate Eq. (5a) by parts to obtain:

$$\frac{1-\nu}{G}\left[p(r_o,t)-\sigma_c\right]=\frac{1}{\pi}\int_0^a \gamma_D(r_o,r)\left[\delta(r,t)-\delta(r_o,t)\right]dr+\frac{1}{\pi}\gamma(r_o,a)\delta(r_o,t)\,, \tag{6a}$$

$$\gamma_D(r_o,r)\equiv d\gamma(r_o,r)/dr\,, \tag{6b}$$

given $\delta(a,t)=0$ and $\gamma(r_o,0)=0$.

Assuming a stationary crack and time-independent influence function $\gamma(r_o,r)$, we differentiate Eq. (6a) with respect to time:

$$\frac{1-\nu}{G}\dot{p}(r_o,t)=\frac{1}{\pi}\int_0^a \gamma_D(r_o,r)\left[\dot{\delta}(r,t)-\dot{\delta}(r_o,t)\right]dr+\frac{1}{\pi}\gamma(r_o,a)\dot{\delta}(r_o,t)\,. \tag{7}$$

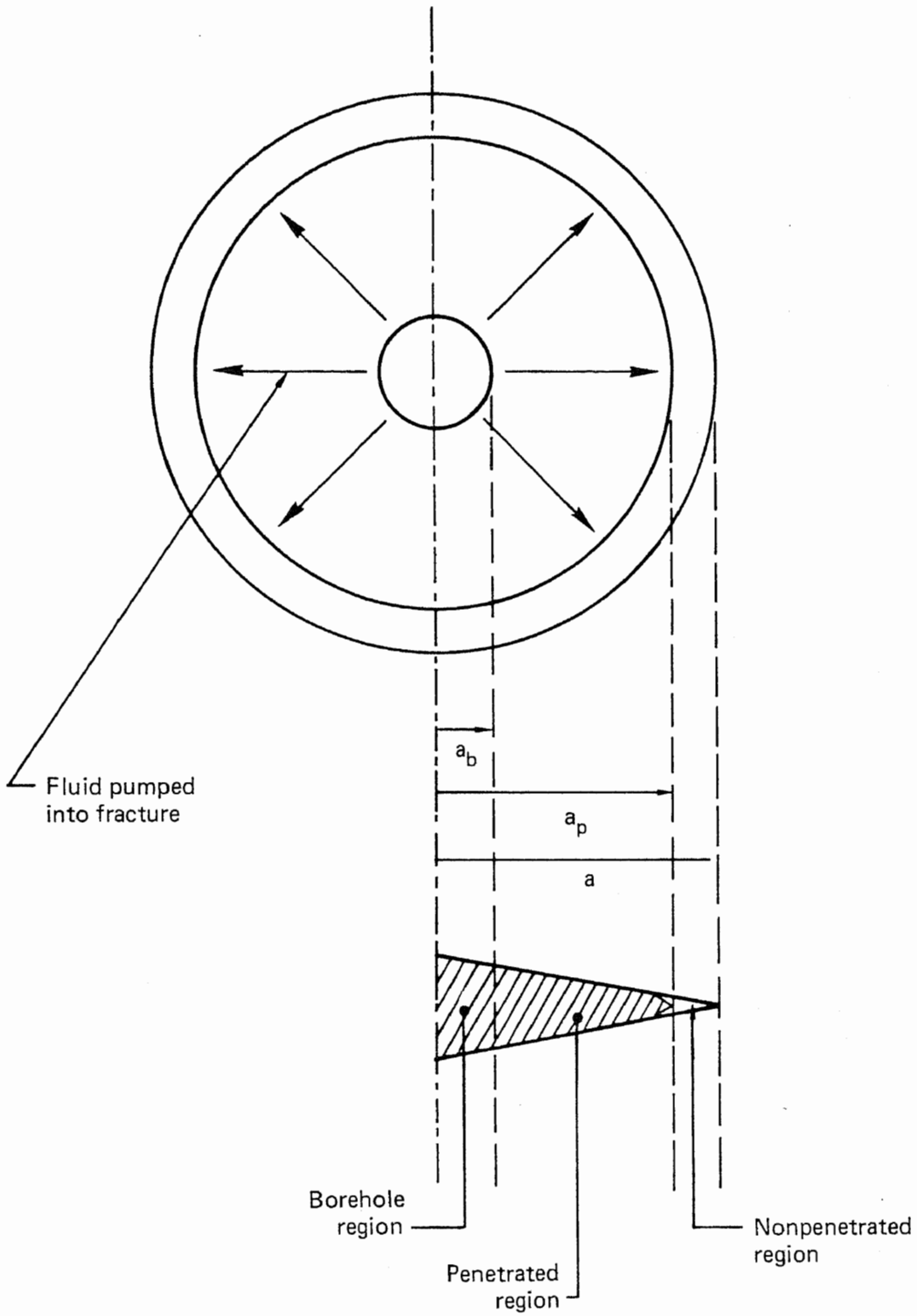

FIG. 7. A circular propagating hydrofrac and its cross section, showing modeling variables.

This is the equation provided by elasticity. The conservation of mass, and the simplest fluid flow model—Poiseuille flow of a Newtonian fluid—also require that, where fluid flow has fully penetrated (i.e., where $a_b < r < a_p$),

$$\hat{\eta}\,\dot{\delta}(r,t) = \frac{1}{r}\frac{\partial}{\partial r}\left[r\delta^3\frac{\partial p}{\partial r}\right](r,t)\ , \tag{8}$$

where $\hat{\eta}$ is the effective viscosity.

For these conditions, a_b is an effective radius, not necessarily the actual radius of the borehole used in the physical counterpart of the models.* To pose the problem well, we take pressure to be known in the borehole and in the nonpenetrated region (where fluid has not yet reached $a_p < r < a$). Thus:

$$p(r,t) = \begin{cases} p_o & ,\ 0 \leqslant r < a_b & \text{(9a)} \\ p(r,t) & ,\ a_o \leqslant r < a_p & \text{(9b)} \\ 0 & ,\ a_p \leqslant r < a\ , & \text{(9c)} \end{cases}$$

where p_o is the borehole pressure and $p(r,t)$, for $a_b \leqslant r < a_p$, is dictated by elasticity and fluid flow [i.e., by Eqs. (7) and (8)]—except that an initial pressure distribution is assumed for $t=0$.

To solve Eqs. (7) and (8), we first nondimensionalize according to

$$r \leftarrow \frac{r}{a}\ ,\ r_o \leftarrow \frac{r_o}{a}\ ,\ p \leftarrow \frac{p}{p_o}\ ,\ \delta \leftarrow \frac{G\delta}{p_o a}\ ,$$

then approximate the time derivatives as

$$\dot{p} = \frac{{}^{t+\Delta t}p - {}^{t}p}{\Delta t}\ ,\quad \dot{\delta} = \alpha\,{}^{t+\Delta t}\dot{\delta} + (1-\alpha)\,{}^{t}\dot{\delta}\ , \tag{10}$$

where α is chosen to give maximum stability (as in the two dimensional analyses[7]). Finally, we map the domain from $0 \leqslant r \leqslant 1$ to $-1 \leqslant x \leqslant 1$ using

$$x = 2r - 1\ ,\quad r = \frac{1}{2}(x+1)\ , \tag{11}$$

so that we can directly apply integration formulae and techniques for differentiation developed in the plane strain models.† After these manipulations, Eq. (7) becomes

---

*A finite borehole size is necessary because $1/r$ in Eq. (8) would cause a singularity in p for any nonzero injection rate; this feature makes the circular crack more complicated than the plane problem.

†This mapping is justified by the facts that: (a) the integration formulae, based on the Chebyshev polynomials, apply to integrals over the domain $[-1, +1]$, and (b) the derivative of any function is obtained by termwise differentiation after expanding the function into a series of Chebyshev polynomials of the first kind, whose domain is $[-1, +1]$. Another approach is to exploit the symmetry of the problem and to impose it on the integration and differentiation formulae. This is the equivalent to using even-ordered Chebyshev polynomials when expanding functions of interest. However, we encountered singularities and the solution oscillated when this approach was used.

$$ {}^{t+\Delta t}p(x_o) - {}^{t}p(x_o) = \frac{\alpha\Delta t}{2\pi} \int_{-1}^{+1} \Gamma_D(x_o,x)^{t+\Delta t}\left[\dot{\delta}(x) - \dot{\delta}(x_o)\right]dx + \frac{\alpha\Delta t}{\pi}\,\Gamma(x_o,1)^{t+\Delta t}\,\dot{\delta}(x_o) $$

$$ + \frac{(1-\alpha)\Delta t}{2\pi} \int_{-1}^{+1} \Gamma_D(x_o,x)^{t}\left[\dot{\delta}(x) - \dot{\delta}(x_o)\right]dx + \frac{(1-\alpha)\Delta t}{\pi}\,\Gamma(x_o,1)^{t}\,\dot{\delta}(x_o)\ , \qquad (12a) $$

$$ \Gamma_o(x_o,x) \equiv \gamma_D(r_D,r)\ , \qquad \Gamma(x_o,1) \equiv \gamma(r_o,1)\ . \qquad (12b) $$

In the region where fluid has penetrated ($a_b = r < a_p$), from Eq. (8),

$$ \tau_c\,\dot{\delta}(x) = \frac{8}{x+1}\left[\frac{x+1}{2}\,\delta^3 p'\right]'(x)\ , \qquad \tau_c = \frac{\hat{\eta}}{G}\left(\frac{G}{p_o}\right)^3\ , \qquad (13) $$

where τ_c ($\equiv 1$, without loss of generality) is the characteristic time, and the prime represents spatial differentiation with respect to x, the dimensionless mapped variable.

We are now ready to approximate integrals using Gauss-Chebyshev formulae and to expand functions in terms of Chebyshev series, so as to find derivatives by termwise differentiation. Since this procedure is exactly analogous to that performed in two-dimensional modeling,[8] we will present the final form of the equations without the details. Equation (12a) becomes

$$ [A]\left\{{}^{t+\Delta t}p\right\} - \alpha\Delta t\,[K]\left\{{}^{t+\Delta t}\dot{\delta}\right\} = [A]\left\{{}^{t}p\right\} + (1-\alpha)\,\Delta t\,[K]\left\{{}^{t}\dot{\delta}\right\}\ , \qquad (14a) $$

$$ [A]_{ik} = \frac{2}{N}\left[\frac{1}{2} + \sum_{\ell=1}^{N} T_\ell(x_i)T_\ell(t_k)\right]\ , \qquad (14b) $$

$$ [K]_{ik} = \frac{1}{2N}\,\Gamma_D(x_i,t_k)\sqrt{1-t_k^2} $$

$$ - \frac{1}{2N}\left\{\sum_{j=1}^{N}\Gamma_D(x_i,t_j)\sqrt{1-t_j^2}\right\}\left\{\frac{2}{N}\left[\frac{1}{2} + \sum_{\ell=1}^{N} T_\ell(x_i)T_\ell(t_k)\right]\right\} $$

$$ + \Gamma(x_i,1)\left\{\frac{2}{N}\left[\frac{1}{2} + \sum_{\ell=1}^{N} T_\ell(x_i)\,T_\ell(t_k)\right]\right\}\ , \qquad (14c) $$

$$ t_{j,k} = \cos\frac{[2(j,k)-1]\pi}{2N}\ , \qquad j,k = 1,\ldots,N\ , \qquad (14d) $$

$$ x_i = \cos\frac{i\pi}{N}\ , \qquad i = 1,\ldots,N-1\ . \qquad (14e) $$

Points t_k and x_i are the zeroes of the N^{th}-order Chebyshev polynomials, first and second kind, respectively. Therefore, we have N–1 equations and 2N unknowns, namely, ${}^{t+\Delta t}p(t_k)$ and ${}^{t+\Delta t}\dot{\delta}(t_k)$, $Y_k = i, \ldots, N$. To close the system, we need N+1 more equations. These are provided by Eqs. (9), (13), and the condition that the opening at the crack tip is zero, namely, ${}^{t+\Delta t}\dot{\delta}(1) = 0$.

From Eqs (9a) and (9c),

$$ {}^{t+\Delta t}p(t_k) = \begin{cases} 0\,, & k = 1, \ldots, M \\ \\ 1\,, & k = J+1, \ldots, N \end{cases} \tag{15} $$

where M is the number of t_k points in the nonpenetrated region, and J–M is the number of t_k points in the penetrated region.

Equation (13) gives

$$ \tau_c \left\{ \dot{\delta}(t_k) \right\} = [B] \left\{ p(t_s) \right\}, \; t_{k,s} = \cos[2(k,s)-1]\pi/2N \,, \tag{16a} $$

$$ [B]_{k,s} = \left(\frac{8}{t_k+1}\right)\left(\frac{2}{N}\right)\sum_{n=1}^{N} T_n'(t_k) \sum_{m=1}^{N} T_n(t_m) \left(\frac{t_m+1}{2}\right)\delta^3(t_m) $$

$$ \times \left(\frac{2}{N}\right)\sum_{\ell=1}^{N} T_\ell(t_m) T_\ell(t_s) \qquad k = M+1, \ldots, J\,. \tag{16b} $$

Finally, crack-tip closure provides the last condition to complete the system of algebraic equations,

$$ \frac{2}{N}\sum_{k=1}^{N}\left[\frac{1}{2} + \sum_{\ell=1}^{N} T_\ell(1)\, T_\ell(t_k)\right] {}^{t+\Delta t}\delta(t_k) = 0\,. \tag{16c} $$

The procedure for tracing pressure evolution starts by specifying an initial pressure distribution and crack opening [which is obtained from either Eq. (5) or (6) with the specified initial pressure as the forcing term]. Then the new pressure and new time rate of crack opening (viz, ${}^{t+\Delta t}p$ and ${}^{t+\Delta t}\dot{\delta}$) are computed from Eqs. (14) and (16) by using a standard equation solver routine; more efficient approaches will be sought in the future. The crack opening is obtained as:

$$ {}^{t+\Delta t}\delta = {}^{t}\delta + \frac{\Delta t}{\tau_c}\left[\alpha\, {}^{t+\Delta t}\dot{\delta} + (1-\alpha)\, {}^{t}\dot{\delta}\right]\,. \tag{17} $$

The typical results shown in Figs. 8 and 9 indicate the effect of size of the nonpenetrated zone, and fineness of the mesh.

Figure 8 shows results obtained using 10 t_k points over the domain [0,1] with $\alpha = 1$, $\Delta t = 0.25\,\tau_c$, a borehole radius of 0.1, and the fluid front at $a_p = 0.8536a$. The initial pressure distribution was taken to be linear over the range $a_b < r < a_p$. Figure 8a shows how pressure builds up with time. Because the crack is not completely filled, the pressure does not approach a uniform distribution, as it did in the corresponding fluid filled, two dimensional crack.[7] A sink at the fluid front takes just enough fluid to keep the front from moving,

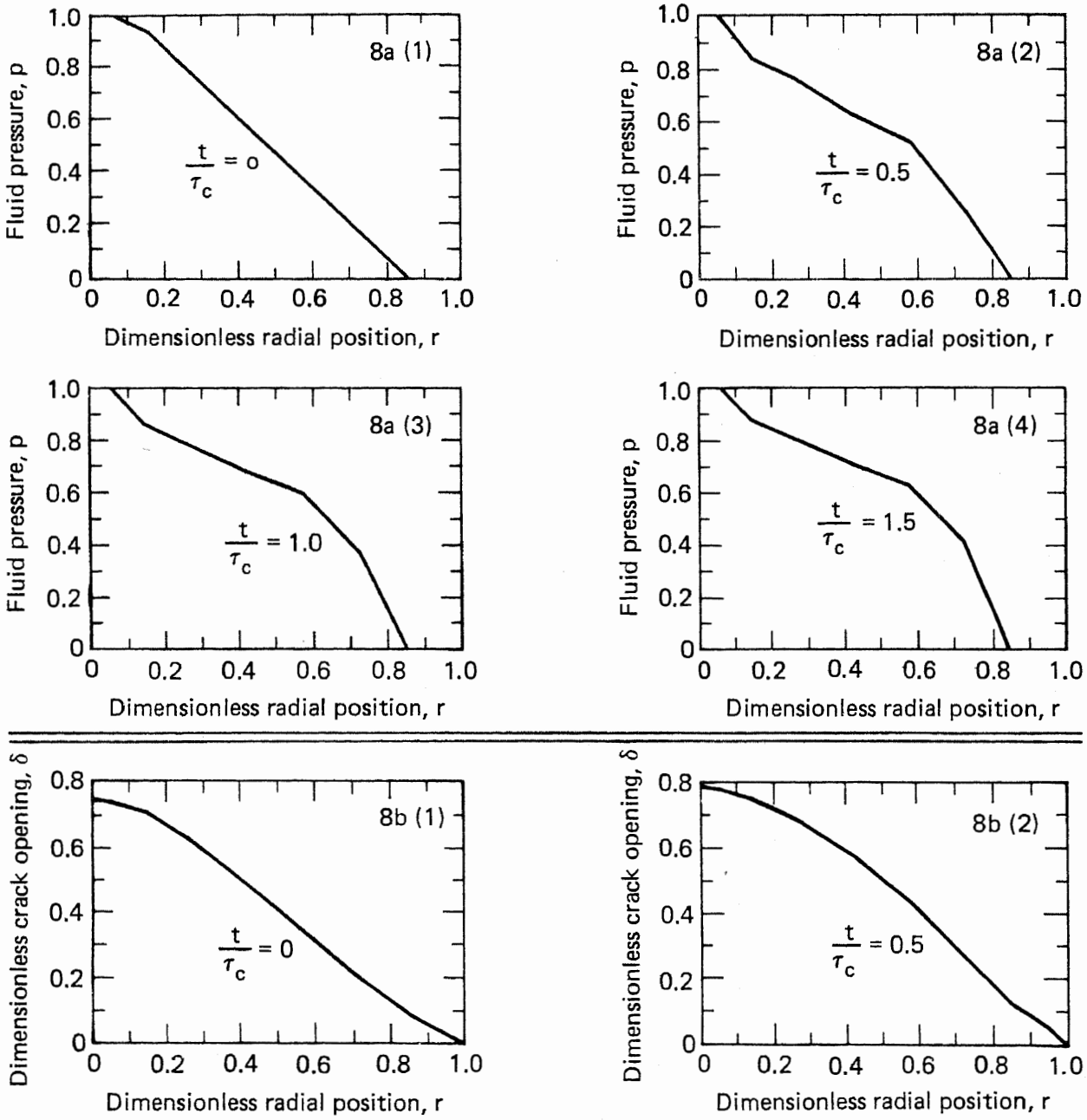

FIG. 8. Curves showing the evolution of the frac-fluid pressure and crack opening with fixed fluid front and crack tip, using N = 10, $a_b = 0.1a$, $a_p = 0.8536a$, $\Delta t = 0.25\ \tau_c$, and a linear initial pressure distribution. Figure 8a shows p; 8b shows δ; 8c shows $\dot{\delta}$.

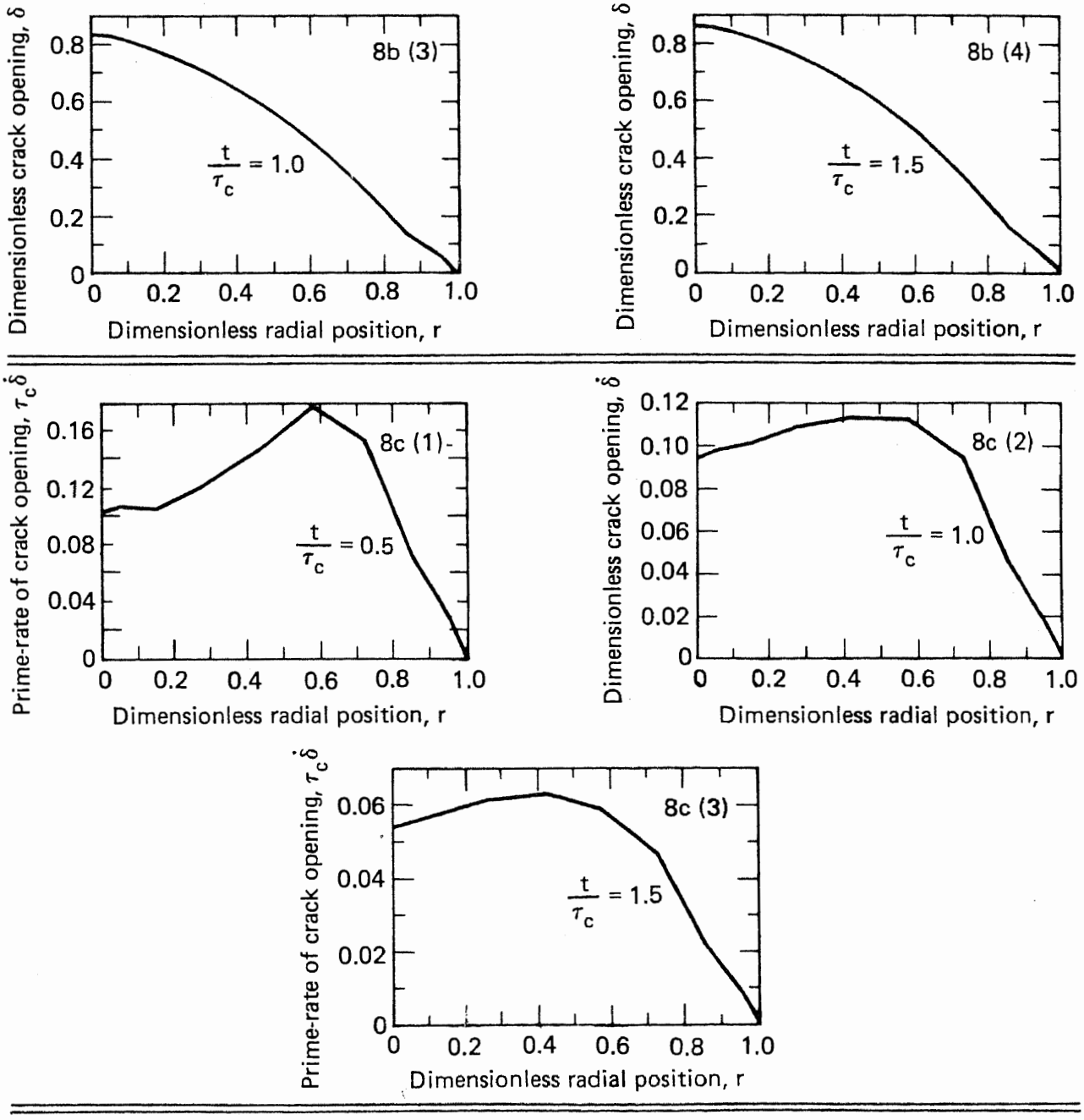

FIG. 8. (Concluded.)

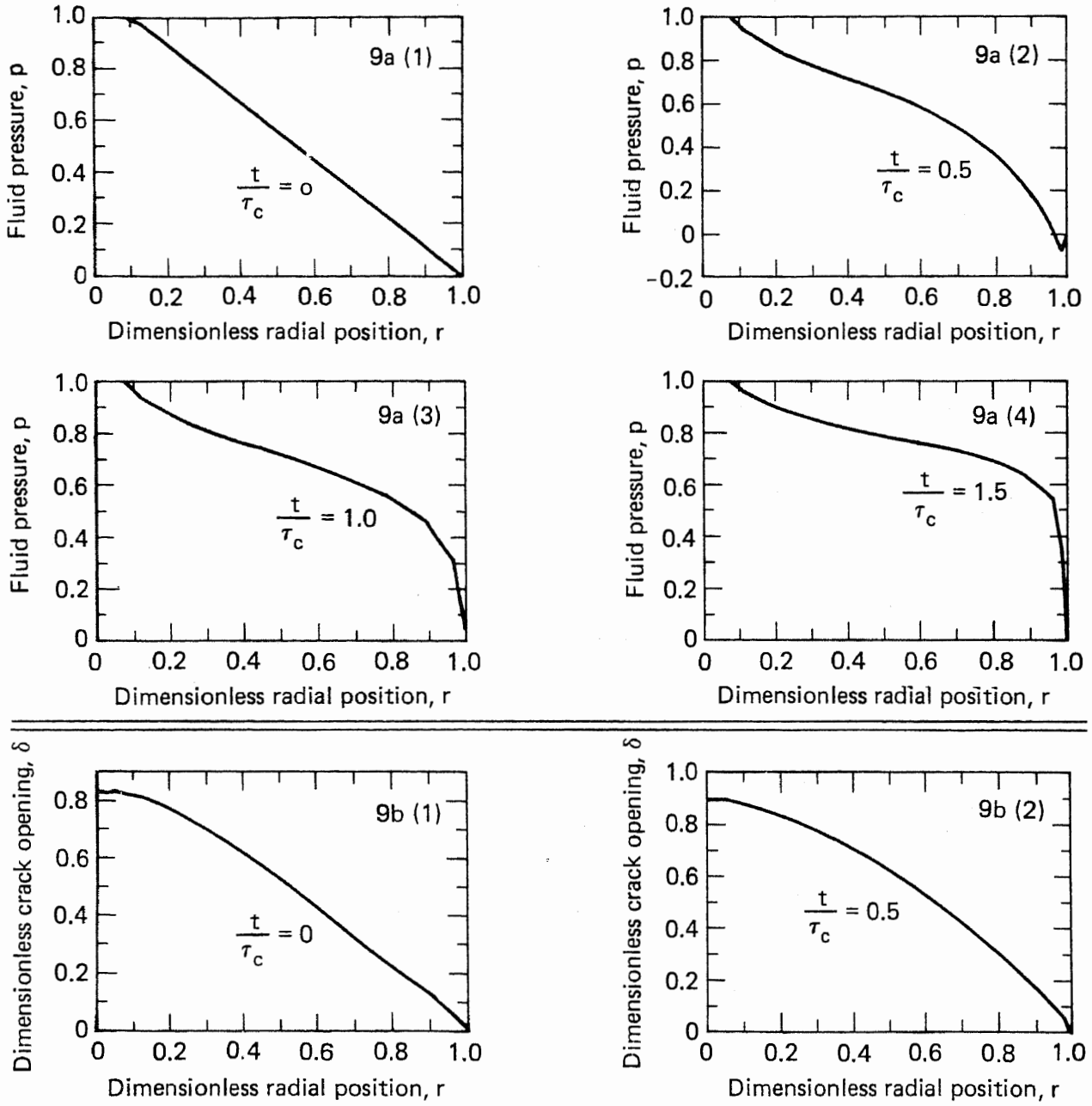

FIG. 9. Plots of pressure, crack opening and its time rate for the frac-fluid pressure evolution with fixed fluid front and crack tip, using N = 20, $a_b = 0.1a$, $a_p = 0.9985a$, $\Delta t = 0.25\ \tau_c$, and a linear initial pressure distribution. Figure 9a shows p; 9b shows δ; 9c shows $\dot{\delta}$.

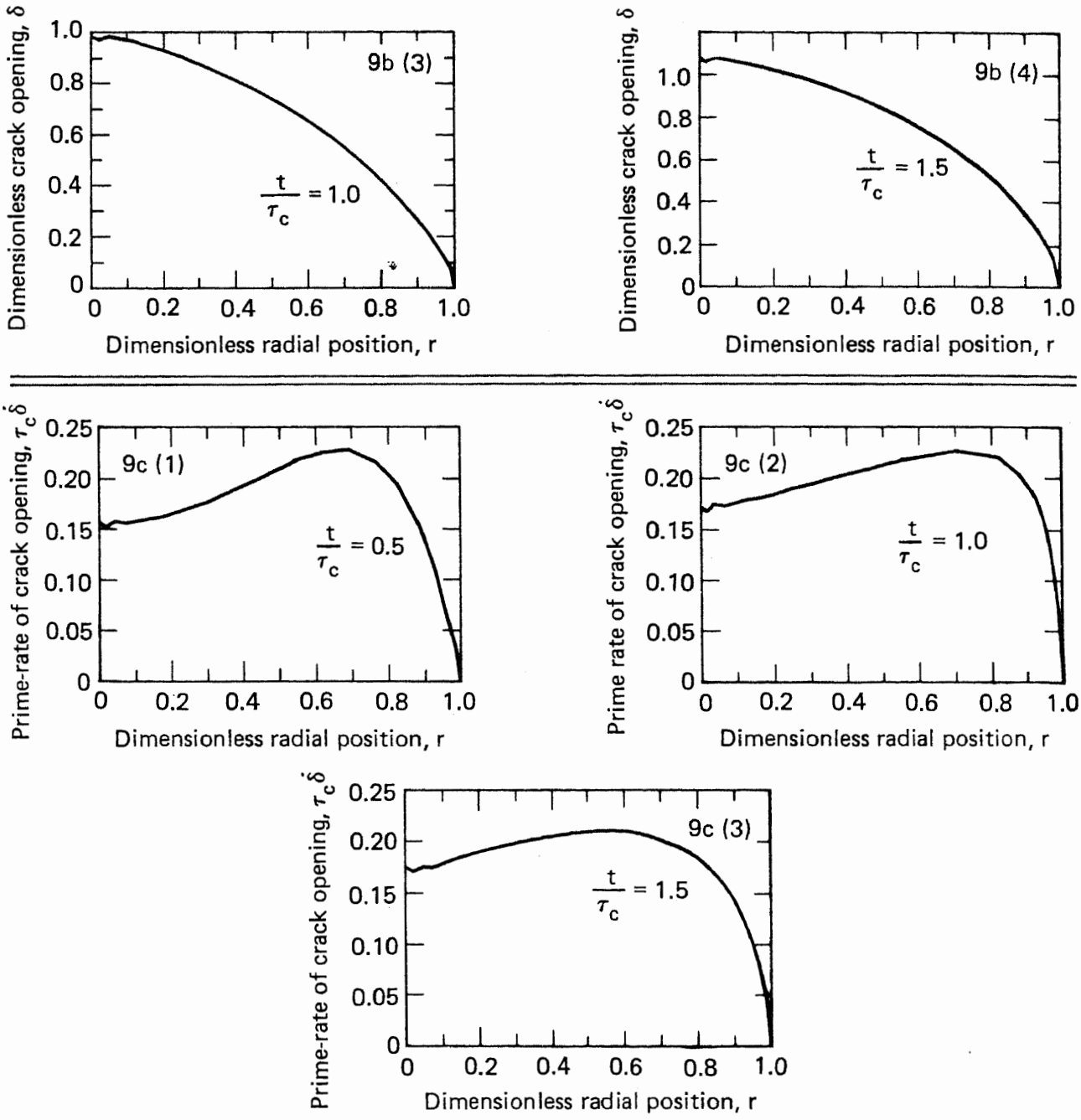

FIG. 9. (Concluded.)

thus maintaining conservation of mass, and also prevents the pressure from building up to a uniform distribution. Figure 8b shows the crack opening δ, and Fig. 8c shows its time rate $\dot{\delta}$. Note that the magnitude of $\dot{\delta}$ decreases with time.

Figure 9 shows results of a run similar to the run shown in Fig. 8. In Fig. 9 there are 20 t_k points and the fluid front is at $a_p = 0.9985a$, so that the crack is almost completely filled. Again we find that pressure builds up with time and has essentially reached a steady state when $t = 1.5\,\tau_c$ (Fig. 9a). The crack opening is smoother in the Fig. 9 run (owing to a smaller nonpenetrated region), but the rate of crack opening has a similar shape for both runs. This shape is the best interpretation of the pressure distributions claimed in the literature as solutions to the propagating hydrofrac problem. (These solutions unfortunately neglect the crack opening term, so it is not correct to use them for design purposes.[9,10])

We have also tested the effects of different values for α and Δt. Conclusions correspond to those obtained in two-dimensional studies: $\alpha = 1.0$ gives most stability, and Δt of $0.1\,\tau_c$ (or even larger) is quite sufficient for accurate tracing of pressure evolution.

Fluid Front Advancement in a Stationary Crack

The fluid front is now allowed to move, while the frac-fluid pressure evolves. At any instant of time, t, the geometry of the problem (Fig. 7) and the governing equations [Eqs. (7), (8), and (9)] remain constant. Only one additional piece of information is needed to account for the motion of the fluid front. This is the front's velocity, $\dot{a}_p$, which is given by assuming Poiseuille flow to be

$$\hat{\eta}\,\dot{a}_p = -\left[\delta^2\,\frac{\partial p}{\partial r}\right](a_p) \tag{18a}$$

or, in dimensionless and discretized form,

$$\dot{x}_p = -\frac{2}{\tau_c}\,\delta^2(x_p)\left\{\frac{2}{N}\sum_{k=1}^{N}\sum_{\ell=1}^{N} T'_\ell(x_p)\,T_\ell(t_k)\,p(t_k)\right\}\,, \tag{18b}$$

where $x_p = 2\,a_p - 1$ is the position of the front in the mapped variable, $x\epsilon[-1, +1]$.

To solve:

1. Specify an initial pressure distribution.
2. Solve for the initial crack opening, using Eq. (6).
3. Calculate the velocity of the fluid front with Eq. (18).
4. Determine a time-step size Δt so as to bring the fluid front from one nodal point t_k to another just ahead, i.e., to t_{k-1}.
5. Set up Eqs. (14) and (16) as before and compute the new pressure ${}^{t+\Delta t}p$, rate of crack opening ${}^{t+\Delta t}\dot{\delta}$, and the new crack opening ${}^{t+\Delta t}\delta$.

Steps 3 through 5 are repeated to march forward in time.

Results from a sample run, obtained with $\alpha = 1.0$, $a_b = 0.1$, and 20 nodal points, are shown in Fig. 10. Initially the fluid front is at $a_p = 0.6913a$ and the pressure distribution is taken to be linearly varying in the penetrated region. Note that the pressure distribution builds up and becomes steeper near the fluid front, and that the shape of the pressure distribution after 6 time steps ($t/\tau_c = 6.1117$) is similar to that shown in Fig. 9a(4). Because the fluid-front velocity is slow at first, the first time-step size is large ($3.7596\,\tau_c$), allowing motion to the next nodal point of the discrete mesh. The scheme is stable enough, however, to give a pressure curve comparable to the curve obtained with a stationary frac-fluid front [Fig. 9a(4)]. The remaining curves (Figs. 9b and 9c) are the crack and its rate of opening as a function of time. Note that the rate of crack opening, $\dot{\delta}$, (Fig. 9c) is comparable to the two dimensional fluid front advancement problem[7] and in both cases $\dot{\delta}$ has a sharp peak near the fluid front.

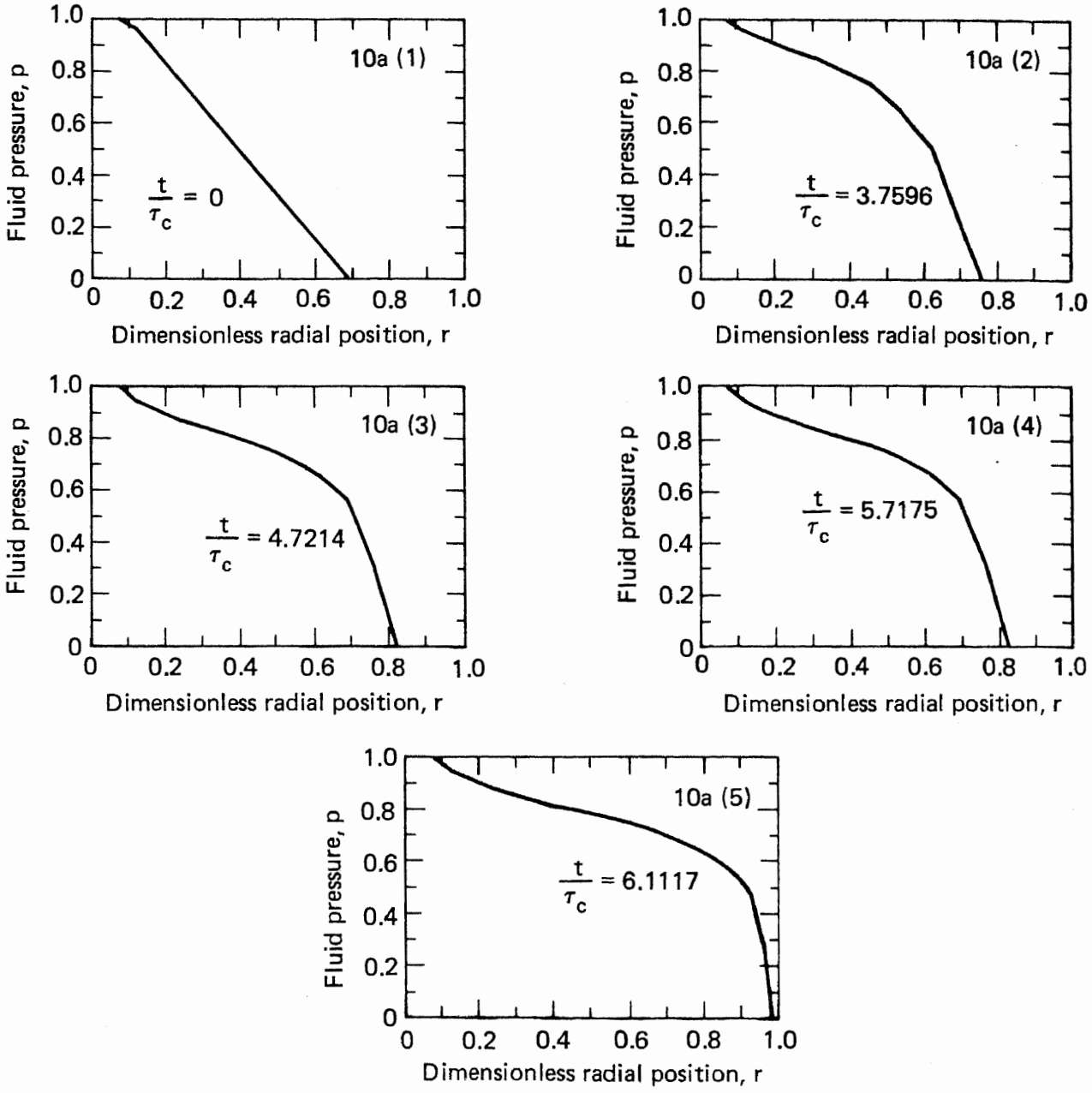

FIG. 10. Plots showing the frac-fluid pressure evolution and fluid front advancement in a stationary circular crack. Note the buildup in pressure and the changes in the shape of the crack opening rate as the fluid front advances. Figure 10a shows p; 10b shows δ; 10c shows $\dot{\delta}$.

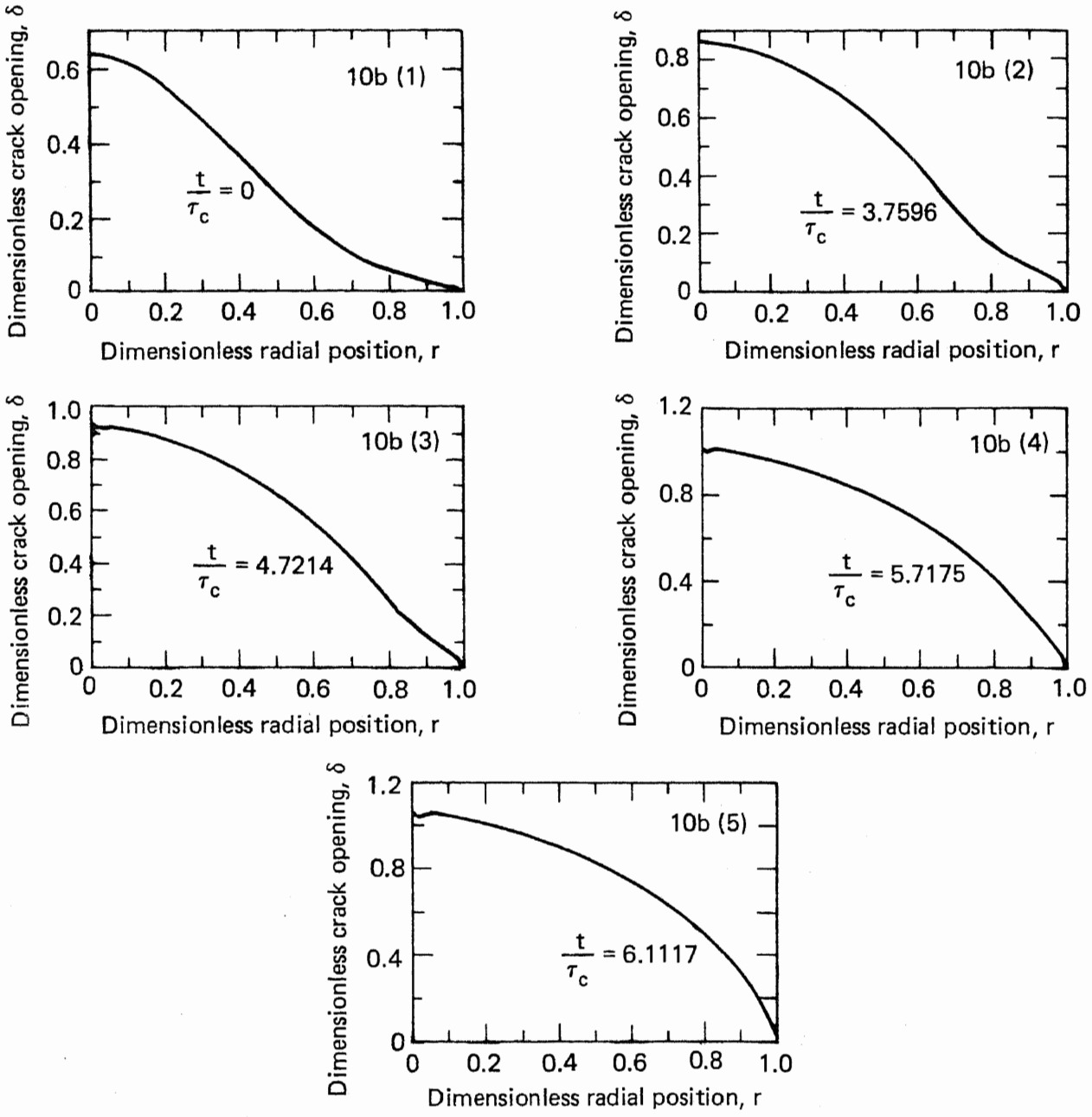

FIG. 10. (Continued.)

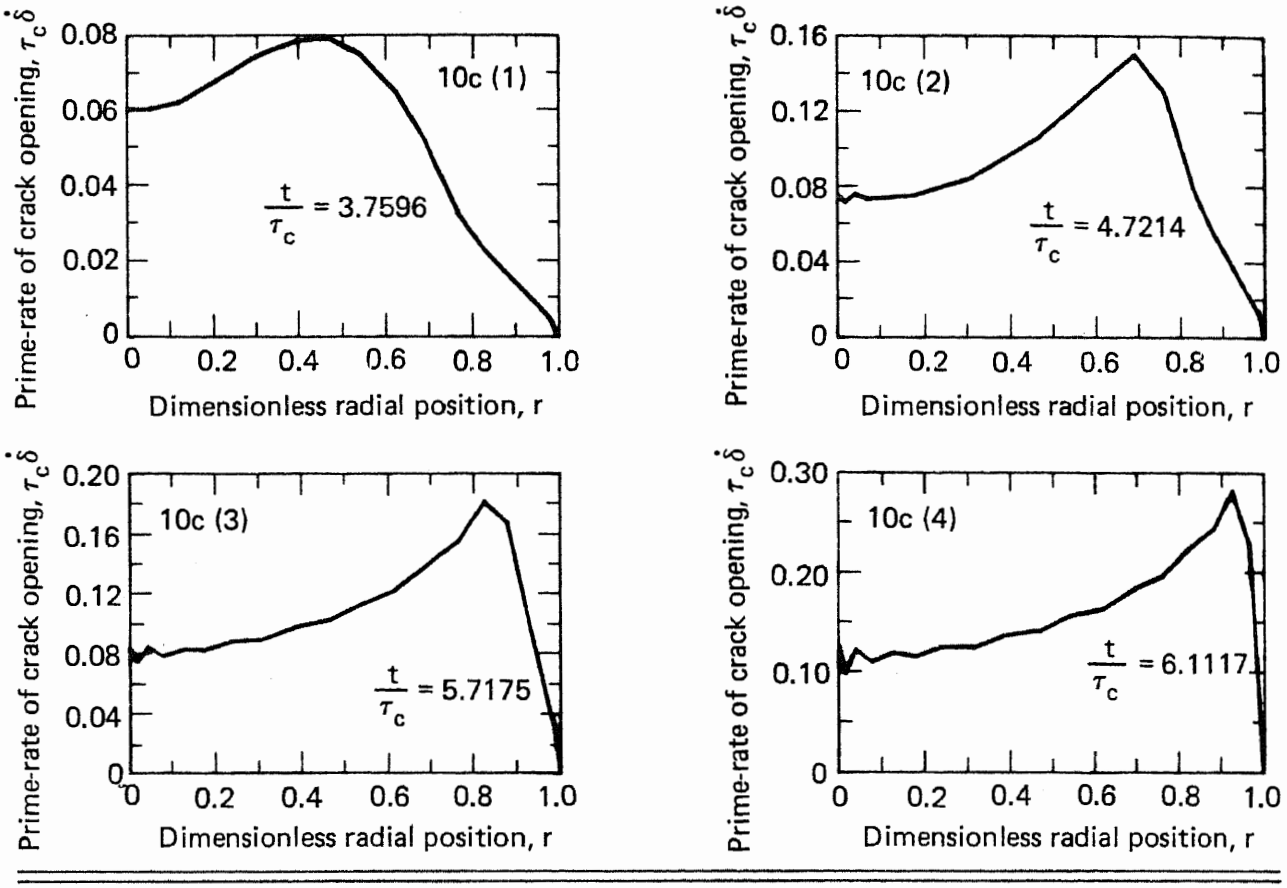

FIG. 10. (Concluded.)

Propagating Crack and Moving Fluid Front

The last major capability needed to model fluid flow propagation of a circular hydrofac is to allow, simultaneously, the evolution of the frac-fluid pressure and the advancement of the fluid front when the crack is propagating. The problem is divided into four parts. (In the beginning, to get an estimate of crack tip velocity, the steps are performed in the indicated sequence; thereafter, steps 2 and 3 are performed before step 1.)

(1) Fix the crack tip and estimate what pressure (${}^{t+\Delta t}p$) and the crack opening (${}^{t+\Delta t}\delta$) will be after fluid motion in the crack, using the methods described and equations given in the discussion above.

(2) Holding fluid fixed, extend the crack suddenly by a specified amount—for example, by 10% of the current crack length t_a. This sudden advance causes the pressure of the frac fluid to change, since the fluid does not have enough time to change distribution, and different pressure is required to provide the same distribution of fluid in the lengthened crack (${}^{t}a + \Delta a$).

Since the distribution of fluid in the extended crack does not change, the crack opening also remains unchanged from the current geometry. Knowing the pressure in the nonpenetrated and borehole regions [given by Eq. (9)], we can solve for the pressure in the penetrated region of the new geometry by applying Eq. (6) at time t, and specifying a mixed boundary value problem: the pressure on $a_h < r < a_p$, and the crack opening on $a_p < r < a$.

Equation (6), in discretized matrix form, with dimensionless variables, applied at time t, then becomes

$$[A]\left\{{}^{t}p\right\} = [K]\left\{{}^{t}\delta\right\} \quad , \tag{19a}$$

where [A] and [K] are given in Eqs. (14b) and (14c).

Note that [A] is the matrix which interpolates a function from nodal points t_k to collocation points x_i, and that [K] is a matrix analogous to stiffness matrices, giving stresses corresponding to crack opening displacements.

(3) Correct the estimates obtained in step (1) by using "partitioning" schemes.

Partition $\{{}^{t}p\}$ and $\{{}^{t}\delta\}$ into three parts corresponding to nonpenetrated, penetrated, and borehole regions, denoted by subscripts n, p, and b, respectively. Equation (19a) then becomes

$$\begin{bmatrix} {}^{n}_{n}K & {}^{n}_{p}K & {}^{n}_{b}K \\ {}^{p}_{n}K & {}^{p}_{p}K & {}^{p}_{b}K \\ {}^{b}_{n}K & {}^{b}_{p}K & {}^{b}_{b}K \end{bmatrix} \begin{Bmatrix} {}^{t}_{n}\delta \\ {}^{t}_{p}\delta \\ {}^{t}_{b}\delta \end{Bmatrix} = \begin{bmatrix} {}^{n}_{n}A & {}^{n}_{p}A & {}^{n}_{b}A \\ {}^{p}_{n}A & {}^{p}_{p}A & {}^{p}_{b}A \\ {}^{b}_{n}A & {}^{b}_{p}A & {}^{b}_{b}A \end{bmatrix} \begin{Bmatrix} {}^{t}_{n}p \\ {}^{t}_{p}p \\ {}^{t}_{b}p \end{Bmatrix} \quad , \tag{19b}$$

where ${}^{n}_{n}K$, ${}^{n}_{p}K$, ${}^{n}_{b}K$, ... , and ${}^{n}_{n}A$, ${}^{n}_{p}A$, ${}^{n}_{b}A$, ... , ${}^{b}_{b}A$ are submatrices of [K] and [A], partitioned in the same manner as $\{{}^{t}p\}$ and $\{{}^{t}\delta\}$. By regrouping, we gather known quantities (${}^{t}_{n}p$, ${}^{t}_{p}\delta$, ${}^{t}_{b}p$) and unknown quantities (${}^{t}_{n}\delta$, ${}^{t}_{p}p$, ${}^{t}_{b}\delta$) into two separate vectors:

$$\begin{bmatrix} {}^{n}_{n}K & -{}^{n}_{p}A & {}^{n}_{b}K \\ {}^{p}_{n}K & -{}^{p}_{p}A & {}^{p}_{b}K \\ {}^{b}_{n}K & -{}^{b}_{p}A & {}^{b}_{b}K \end{bmatrix} \begin{Bmatrix} {}^{t}_{n}\delta \\ {}^{t}_{p}p \\ {}^{t}_{b}\delta \end{Bmatrix} = \begin{bmatrix} {}^{n}_{n}A & -{}^{n}_{p}K & {}^{n}_{b}A \\ {}^{p}_{n}A & -{}^{p}_{p}K & {}^{p}_{b}A \\ {}^{b}_{n}A & -{}^{b}_{p}K & {}^{b}_{b}A \end{bmatrix} \begin{Bmatrix} {}^{t}_{n}p \\ {}^{t}_{p}\delta \\ {}^{t}_{b}p \end{Bmatrix} \quad . \tag{19c}$$

This is the final form of the matrix equation which gives the moving tip (MT) pressure (${}^{t}_{MT}p$) and crack opening (${}^{t}_{MT}\delta$), satisfying the equations of elasticity when the crack front is advanced but no fluid flow is allowed. Note that, in the dimensionless variables, crack length has been used as a scaling factor; each time we extend the crack, all the variables have to be rescaled with respect to crack length. This means that the crack opening, obtained with fixed crack tip, has to be rescaled in both amplitude and position, before it can be inserted into ${}^{t}\delta_p$ in Eq. (19c) as part of the forcing term.

(4) Calculate the crack tip velocity, assuming that the stress intensity factor K is always at the critical value K_c, which may vary with position of the tip as described by its space derivative K_c'. For a penny-shaped crack of radius a, under a normal loading p(r,t) and a confining stress σ_c along its surface, the stress intensity factor is given by [8]

$$K\{p\} \equiv \frac{2}{\pi\sqrt{a}} \int_0^a \frac{rp(r,t)}{\sqrt{a^2 - r^2}}\, dr \,, \quad K = K\{p\} - \sigma_c \sqrt{\pi a} \quad . \tag{20}$$

Setting the time derivative of Eq. (20) to $K_c' \dot{a}$, and performing some integration by parts, obtain an expression for the crack tip velocity scaled to the crack length:

$$\frac{\dot{a}}{a} = \frac{-2K\{\dot{p}\}}{K\{p\} + 2K\{rp'\} - 2aK'_c - \sigma_c\sqrt{\pi a}} \quad . \tag{21}$$

We now have enough information to solve the entire problem of fluid and crack-tip motion. We start with some pressure distribution ${}^{t}p\,(r)$ and crack opening ${}^{t}\delta\,(r)$. These have to satisfy Eq. (6) in the current geometry, which is characterized by the borehole radius ${}^{t}a_b$, the fluid front's position ${}^{t}a_p$, and the crack length ${}^{t}a$ (which serves as a scaling factor). We also assume that we know the velocities of the fluid front and crack tip, ${}^{t}\dot{a}_p$ and ${}^{t}\dot{a}$. These velocities must be consistent with the pressure, ${}^{t}p\,(r)$, and the crack opening, ${}^{t}\delta\,(r)$; and with the time and spatial derivatives of pressure and crack opening in the current geometry, obtained using Eqs. (6)–(9), (18), (19), and (21). With a predetermined extension in crack length, $\Delta a/a$, the time step size is determined as

$$\Delta t = \Delta a / {}^{t}\dot{a} \quad . \tag{22}$$

The size of $\Delta a/a$ depends on the mesh size, i.e., on the distance between nodal points used in the interpolation. We will increase this distance by approximately 10% at each increment, with variations to accommodate fluid front motion from one nodal point to another.

To estimate ${}^{t}\dot{a}$ (for example, on the first time-step of the run), the position of the fixed crack tip is combined with the position of the fixed fluid front to estimate $\dot{a}$. The tip is then advanced with that $\dot{a}$, allowing fluid motion to follow, and $\dot{a}$ is reestimated. This process is repeated until the estimated $\dot{a}$ agrees with the $\dot{a}$ implied by the resulting motion.

At any time step, use the "partitioning" scheme outlined in step (3) to obtain corrected fixed tip (FT) pressure, ${}^{t+\Delta t}_{FT}p$, and crack opening, ${}^{t+\Delta t}_{FT}\delta$ (step 1).

Then extend the crack by Δa and rescale the quantities ${}^{t}_{FT}p$ and ${}^{t}_{FT}\delta$ with respect to the new crack length ${}^{t}a + \Delta a$ (step 3). The solution of Eq. (19) provides the moving tip (MT) pressure, ${}^{t}_{MT}p$, in the new geometry.

We now have two expressions for the time derivative of pressure: ${}_{FT}\dot{p} = ({}^{t+\Delta t}_{FT}p - {}^{t}_{MT}p)/\Delta t$ and ${}_{MT}\dot{p} = ({}^{t}_{MT}p - {}^{t}p)/\Delta t$. Typical plots at these pressures are shown in Figs. 11 and 12.

The first expression, obtained with no crack-tip motion, represents the building up of pressure when fluid flows in a stationary crack, which tends to propagate the crack. The second expression accounts for a "pancake effect," where pressure changes appreciably when the crack is extended suddenly without fluid motion (so that a "pancake" of fluid is frozen in position during the process). The change in pressure typically tends to reduce the stress-intensity factor and thus provides stability so that the crack tip cannot run too far away from the fluid body. The major source of stabilization comes, of course, from the confining stress σ_c, which also acts to close the crack. How effective the confining stress is in stabilizing the crack depends on the amount of stress relative to the excess pressure (borehole pressure minus σ_c). The total time derivative of pressure ${}_{T}\dot{p}$, given by

$${}_{T}\dot{p} = {}_{FT}\dot{p} + {}_{MT}\dot{p} \quad , \tag{23}$$

is used in Eq. (21) to determine a crack tip velocity ${}^{t}\dot{a}_1$. If this value compares reasonably well with the ${}^{t}\dot{a}$ at the beginning of this time step, that is, if $\dot{a}$ vs t is a relatively smooth curve, we proceed with the solution. If not, we take a suitable mean velocity and recalculate the fluid motion, with ${}^{t}_{MT}p$ and ${}^{t}_{MT}\delta$ as initial conditions, until we find an acceptable crack tip velocity. We then interchange the values of pressure, crack opening, and crack tip velocity at times t and $t + \Delta t$. The quantities at time $t + \Delta t$ serve as initial conditions for the next time step.

The procedure on the first time step, to initialize conditions, has to be somewhat expanded. Calculate ${}^{o}_{FT}\dot{p}$, using the specified ${}^{o}p$ as initial condition for the fluid flow [Eq. (14)], and holding the tip fixed. Separately, advance the tip by a suitable amount Δa, and calculate a new pressure ${}^{o}_{MT}p$ with the partitioning scheme of Eq. (19). Using a slightly modified version of Eq. (21), solve for a suitable time step size Δt, without

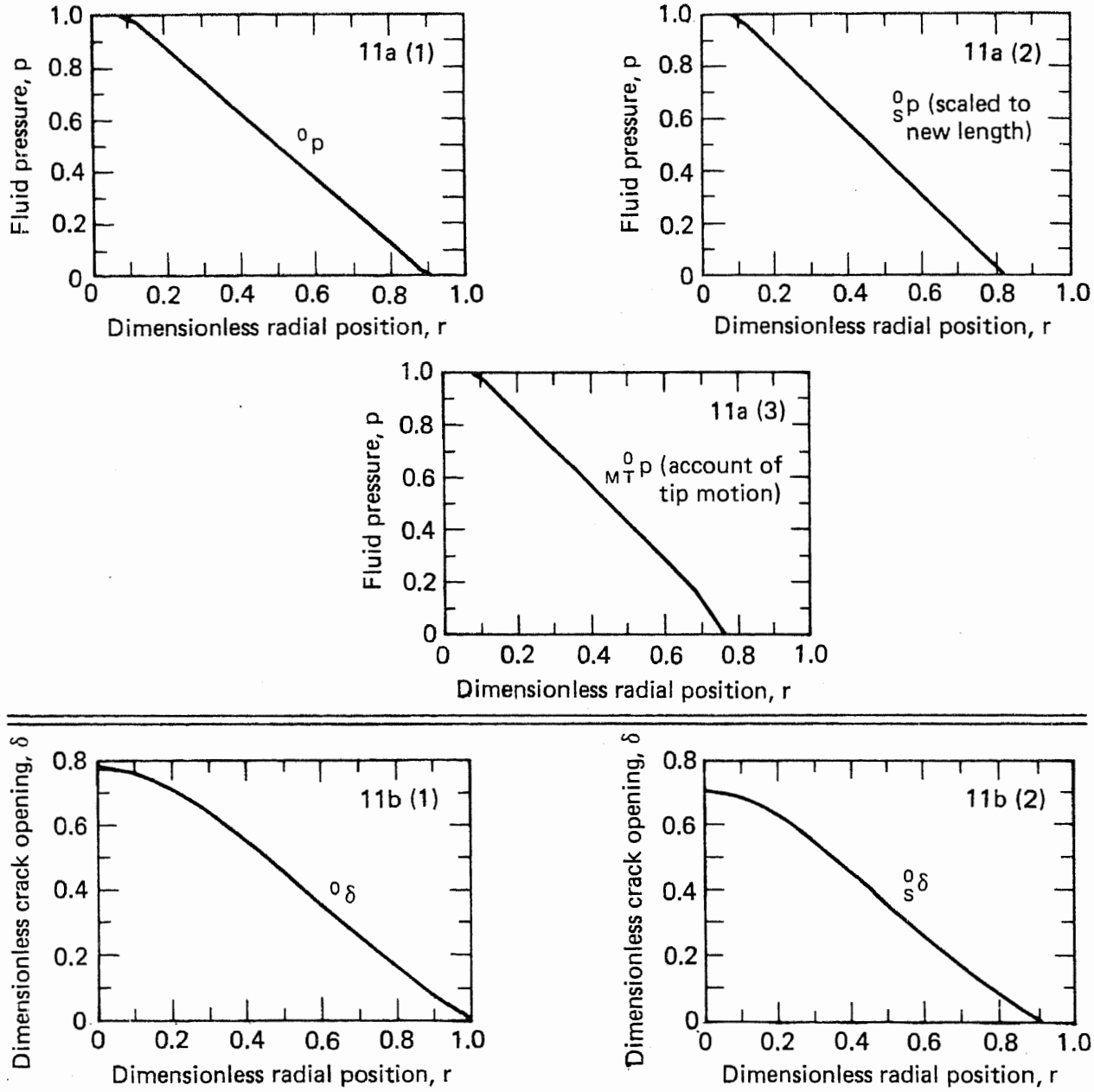

FIG. 11. Plot for a propagating crack with a moving fluid front where we used $a_b = 0.1a$, $a_p = 0.9a$, $\Delta t = 0.1\tau_c$, $\Delta a = 0.1a$, and $N = 20$. Initial pressure distribution is linear. The plots are ^{o}p, $^{o}_{s}p$, $^{o}_{MT}p$, $^{o}\delta$, $^{o}_{s}\delta$, $^{o}_{MT}\delta$, $_{FT}\dot{p}$, $_{MT}\dot{p}$, and $_{T}\dot{p}$ in the order of a through i. The crack tip velocity computed from $_{T}\dot{p}$ is $\dot{a}/a = -0.1505$, which means the crack tip is moving backwards.

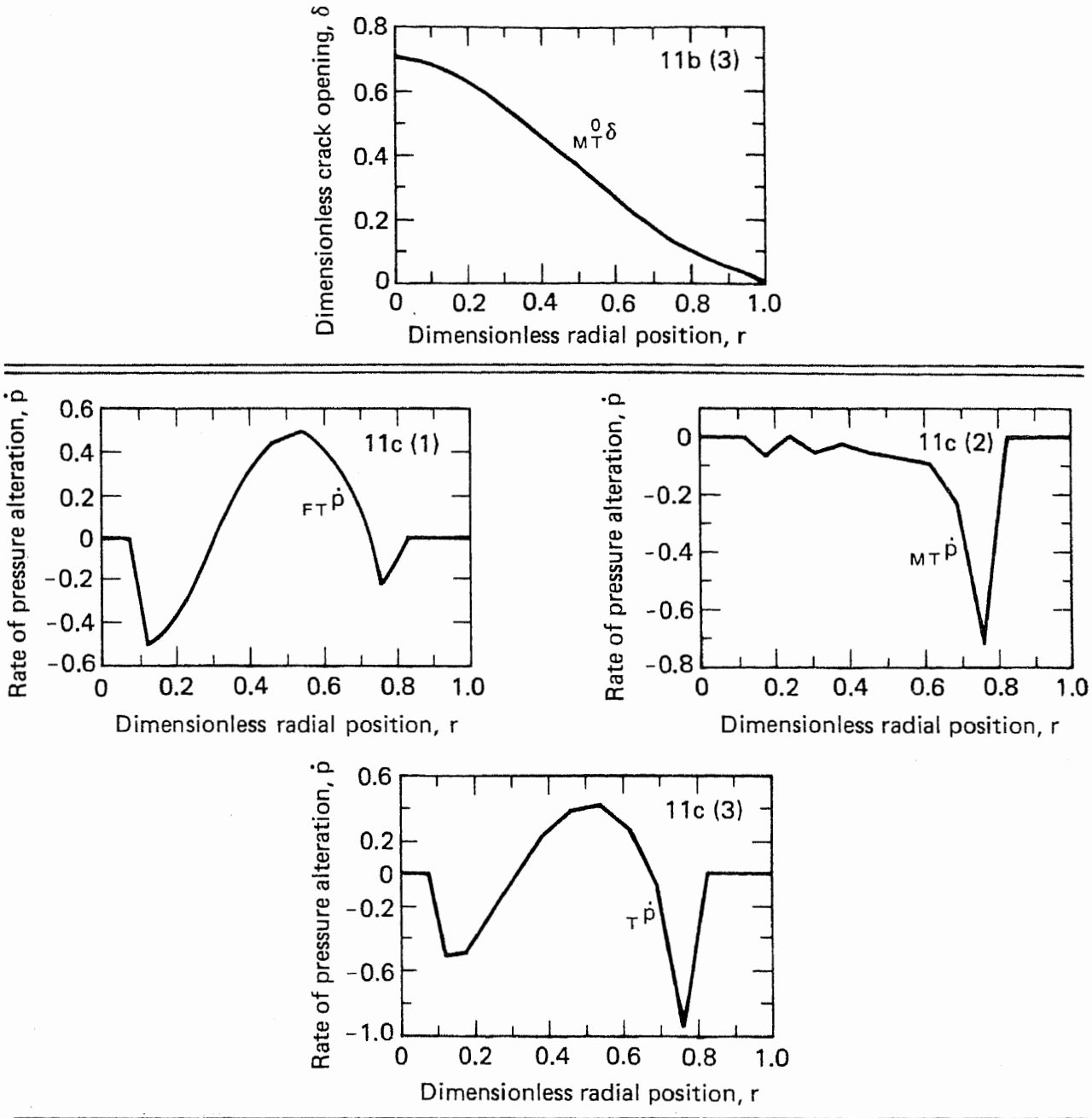

FIG. 11. (Concluded.)

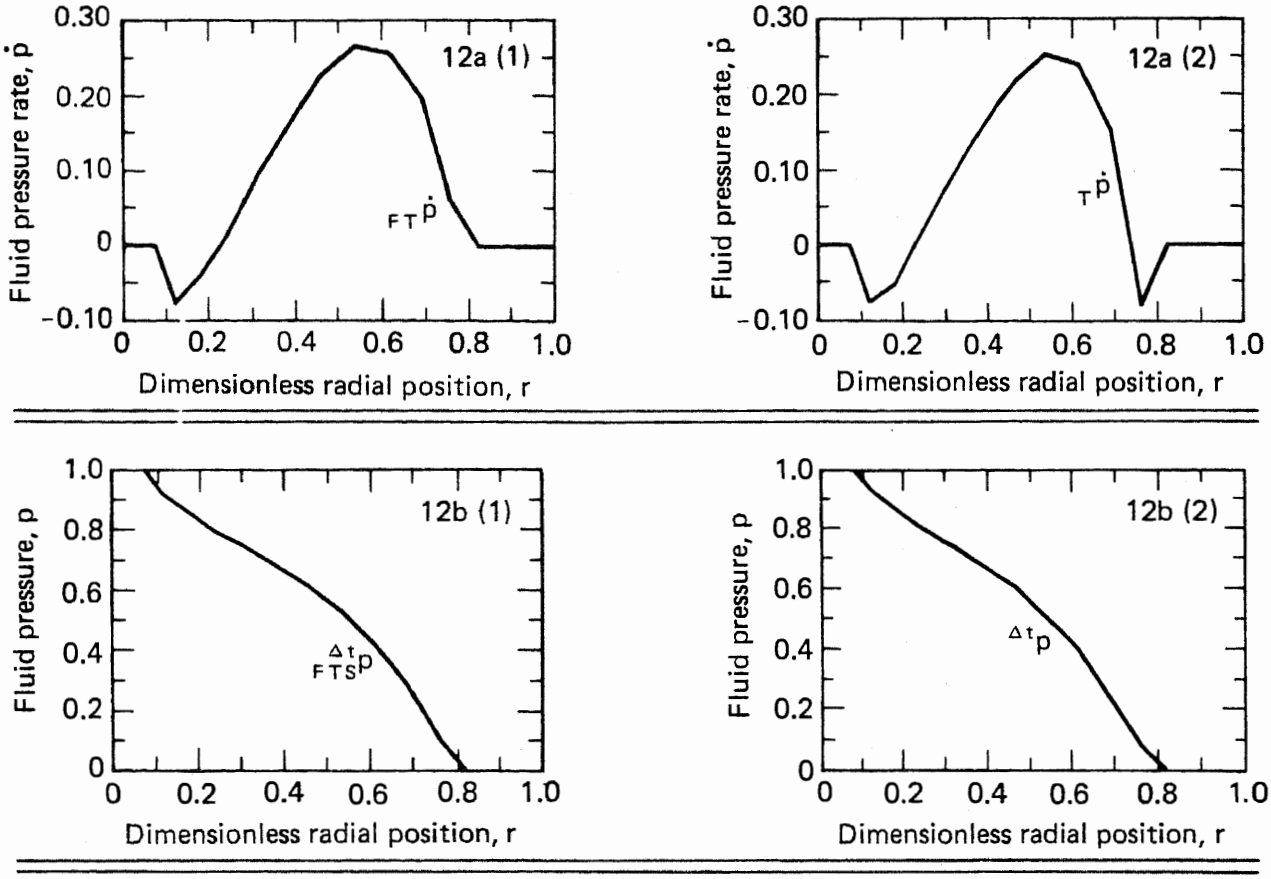

FIG. 12. Plots of $_{FT}\dot{p}$, $_{T}\dot{p}$, $_{FTS}^{\Delta t}p$, $^{\Delta t}p$, and $^{\Delta t}p$ from a propagating crack and moving fluid front where the same conditions given in Fig. 11 are used except $\Delta t = 0.5182\ \tau_c$, which is the time step size required to extend the crack by 10%, and is calculated using the results shown in Fig. 11. Note that $_{FT}\dot{p}$ is positive at the fluid front and $_{FTS}^{\Delta t}p$ and $^{\Delta t}p$ are very close to each other. The crack tip velocity is $\dot{a}/a = 0.2284$, which is within 20% of $\Delta a/\Delta t = 0.1930$.

iteration—which should give a $\Delta a/\Delta t$ consistent with the actual value implied by the overall process. Equation (21) can be written as

$$K\{_{FT}\dot{p}\} + K\{_{MT}\dot{p}\} = \frac{-\dot{a}}{2a}\left[K\{p\} + 2K\{rp'\} - 2aK_c' - \sigma_c\sqrt{\pi a}\right] . \tag{24a}$$

Since by definition

$$K\{_{MT}\dot{p}\} = K\{_{MT}^{t}p - {}^{t}p\}/\Delta t \quad , \quad \dot{a} = \Delta a/\Delta t \quad , \tag{24b}$$

Eq. (24a) gives

$$\Delta t = \frac{-1}{K\{_{FT}\dot{p}\}}\left[K\{_{MT}^{t}p - {}^{t}p\} + \frac{\Delta a}{2a}\left(K\{p\} + 2K\{rp'\} - 2aK_c' - \sigma_c\sqrt{\pi a}\right)\right] . \tag{25}$$

Once this optimal time step size Δt is obtained, use the resulting $\Delta a/\Delta t$ as the first estimate for $\dot{a}$, and start the solution procedure leading to Eq. (23), from which a new $\dot{a}$ is obtained. Use a suitable (e.g., geometric) mean of these velocities until successive calculations agree, that is, until velocities are close enough to each other so that the new pressure ${}^{t+\Delta t}p$ and crack opening ${}^{t+\Delta t}\delta$, satisfying the equations from elasticity [Eq. (6)], fluid flow [Eq. (8)], and propagation criterion [Eq. (21)], can be used to march ahead another time step.

Results of calculations for a propagating crack with a moving fluid front are shown in Figs. 11 and 12. Figure 11 shows the results obtained using $\Delta a = 0.1a$, $\Delta t = 0.1\ \tau_c$, $a_b = 0.1a$, $a_p = 0.9a$, and a linear initial pressure distribution [Fig. 11a(1)]. The quantities obtained, like ${}^{\Delta t}_{FT}p$, ${}^{\Delta t}_{FT}\delta$, and ${}^{\Delta t}_{FT}\dot{\delta}$, have the same characteristics as those described previously. The initial pressure ${}^{o}_{s}p$ [Fig. 11a(2)] and initial crack opening ${}^{o}_{s}\delta$ [Fig. 11b(2)], scaled with respect to the new crack length 1.1a, are fed into the partition scheme to give ${}^{o}_{MT}p$ and ${}^{o}_{MT}\delta \cdot {}^{o}_{MT}p$ is zero in the nonpenetrated region as stated previously, increases from zero at $r = 0.8247a$ to 0.0058 at $r = 0.7613a$, and then rises sharply to an approximately linear distribution in the penetrated region.

The flat section at the end of the ${}^{o}_{MT}p$ curve [Fig. 11a(3)] represents induced suction where, after the sudden extension of the crack, fluid would have been needed to maintain a constant pressure if the fluid front had been allowed to move.

Figure 11c shows plots of the two parts of the derivative of pressure, ${}_{FT}\dot{p}$ and ${}_{MT}\dot{p}$, and their sum, ${}_{T}\dot{p}$. Although no crack tip motion is involved, pressure drops near the interfaces between the borehole, penetrated, and nonpenetrated regions [Fig. 11c(1)]. The pressure also drops near the fluid front. Since the fluid front is stationary, the program cannot advance it ahead to the next nodal point. This results in a sink of fluid at the stationary fluid front, allowing less fluid to go into the crack opening and, hence, causing a slight drop in pressure. This is similar to the mechanism that causes the flat portion in the curve of ${}^{o}_{MT}p$ [Fig. 11a(3)].

These pressure drops may be avoided by starting with an initial pressure distribution which has a larger slope at the fluid front, as happens after some time anyway, or by increasing Δt so that fluid can move further in one time-step.

In any case, Fig. 11 shows pressure increasing over most of the crack, as expected. ${}_{MT}\dot{p}$ is negative (Fig. 11c), which means that when the crack extends, pressure drops. The spike at the fluid front corresponds to the flat in ${}^{o}_{MT}p$, since ${}_{MT}\dot{p} = ({}^{o}_{MT}p - {}^{o}p)/\Delta t$. The stress intensity factors due to these time derivatives of pressure, $K\{{}_{FT}\dot{p}\} = 0.0560$ and $K\{{}_{MT}\dot{p}\} = 0.0867$, are of comparable magnitudes. As they are of opposite sign, they have opposing effects. While $K\{{}_{FT}\dot{p}\}$ tends to propagate the crack, $K\{{}_{MT}\dot{p}\}$ brings the crack tip back and thus stabilizes the solution scheme. When the sum of two parts, ${}_{T}\dot{p} = {}_{FT}\dot{p} + {}_{MT}\dot{p}$, [Fig. 11c(3)] is used in Eq. (21), we obtain a crack tip velocity $\dot{a}/a = -0.1505$. This means the crack is propagating backwards and the initially assumed value of $\dot{a}/a = 1$ is too large. However, Eq. (25) now allows us to calculate an appropriate time step size Δt which will extend the crack by 10%. This value is found to be $0.5182\ \tau_c$, neglecting K_c' and σ_c.

We now start with the same geometry and initial pressure distribution used before and repeat the above procedure with $\Delta t = 0.5182\ \tau_c$. Results are shown in Fig. 12. Since we start with the same initial pressure distribution, the quantities ${}^{o}p$, ${}^{o}\delta$, ${}^{o}_{s}p$, ${}^{o}_{s}\delta$, ${}^{o}_{MT}p$, ${}^{o}_{MT}\delta$ (as depicted in Figs. 11a and 11b) remain the same. Figure 12a(1) shows that part of the time derivative of pressure corresponding to a fixed crack tip. Note that the frac-fluid pressure does not drop near the fluid front anymore (compare with Fig. 11c) because we are using a larger time step size so that fluid has more time to flow. Also, near the borehole, the frac-fluid pressure does not drop as much as in the case using $\Delta t = 0.1\ \tau_c$.

The behavior of ${}_{MT}\dot{p}$ shown in Fig. 12, the part of the pressure alteration caused by crack extension, has the same characteristics as the previous ${}_{MT}\dot{p}$ (see Fig. 11c) with scale reduced by $0.1/0.5812 = 0.1930$. The sum of the two parts ${}_{FT}\dot{p}$ and ${}_{MT}\dot{p}$ is shown in Fig. 12a(2). Using the total value ${}_{T}\dot{p}$ and Eq. (21), we get a crack tip velocity $\dot{a}/a = 0.2284$, which is within 20% of the crack tip velocity we started with ($\dot{a}/a = 0.1930$). Thus, the proposed scheme is successful for calculating the initial crack tip velocity.

Figure 12b shows the new pressures ${}^{\Delta t}_{FTS}p$ and ${}^{\Delta t}p$, corresponding to no crack tip motion and moving crack tip, respectively. The pressure corresponding to fixed crack tip is scaled to the new crack length to allow comparison. The two curves are very close to each other (within 5%).

LABORATORY EXPERIMENTS

Small-scale laboratory experiments are being performed to guide and corroborate the theoretical models. These experiments are not intended to simulate *in-situ* hydraulic stimulation of a reservoir. They are highly idealized experiments in which specific parameters are controlled for comparison with the prediction of the theoretical models. At the present time the results are more qualitative than quantitative with regard to the modeling.

The rocks used in the experiments are Indiana limestone and Nugget sandstone from Utah. These two materials were chosen because they represent two different rock types. The limestone is a porous rock (~15%) relatively weak in compression, and the sandstone is a stronger, less porous (~3%) rock. Some mechanical properties are summarized in Table 1.

Two types of experiments are performed. One of the experiments treats the conditions of load under which a hydraulic fracture will cross an unbonded interface and the other measures the friction between the interface surfaces. These techniques have been described previously[11] but a brief description will be repeated here. The hydraulic fracture experiment is shown in Fig. 13. Here prismatic blocks of the rock to be studied are stacked between the platens of a press. As can be seen in Fig. 13, the sides of the blocks are unconfined so that the load acts only across the interfaces between the blocks. Generally the stack consists of three blocks with the fracturing fluid injected into the center block. The prismatic blocks which are nominally 2 in. × 4 in. × 4 in. are machined flat with opposite faces parallel to insure uniform distribution of the applied load. The fluid is pressurized through an injection tube which is cemented by epoxy in an injection hole drilled into the center of the block. The experiment then consists of pressurizing the fluid until breakdown occurs and observing under which conditions of applied load and interface condition the hydraulic fracture, which is initiated in the block with the injection tube, will cross the interface and enter the adjacent block.

The frictional experiment is shown in Fig. 14. This apparatus consists of a hydraulic vise which squeezes together a sandwich of three blocks. The magnitude of the applied load is measured by a pressure transducer. A vertical ram applies a force to the center block which eventually causes it to slide between the two outer blocks. This load is measured by a load cell. The frictional properties of the interface are then given by the vertical load necessary to initiate motion under a given horizontal load. This frictional property depends upon the preparation of the sliding interface.

TABLE 1. Mechanical properties of rocks.

Material	Strength, MPa	Compressive strength, MPa	Bulk modulus, GPa	Poisson ratio	Initial density, Mg/m^3
Nugget sandstone	3.7–7.5[a] 6.3–8.6[b]	230.0	11.7	.07	2.55
Indiana limestone (dry)	4.7–5.9	62.0	11.3	.115	2.28
Indiana limestone (saturated)	1.9	—	—	—	2.45

Note: See Ref. 11.

[a]Perpendicular to bedding.

[b]Parallel to bedding.

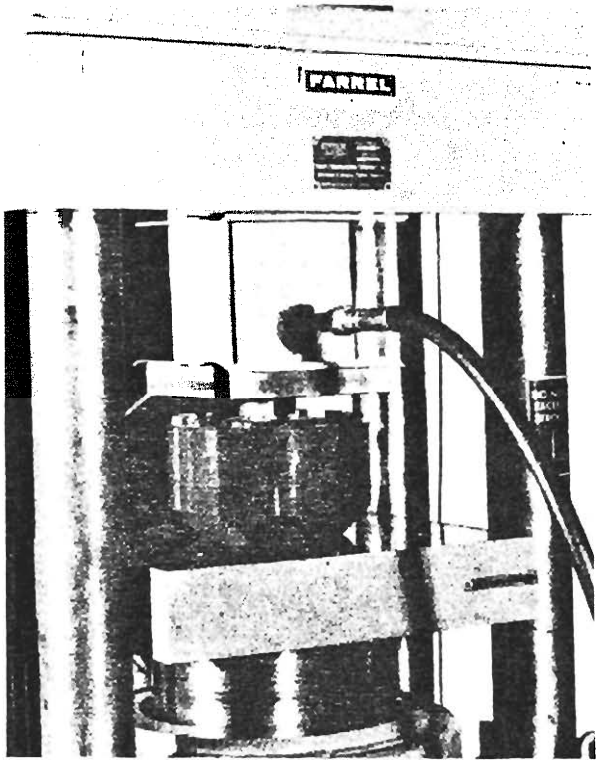

FIG. 13. Hydraulic fracture—interface experimental setup.

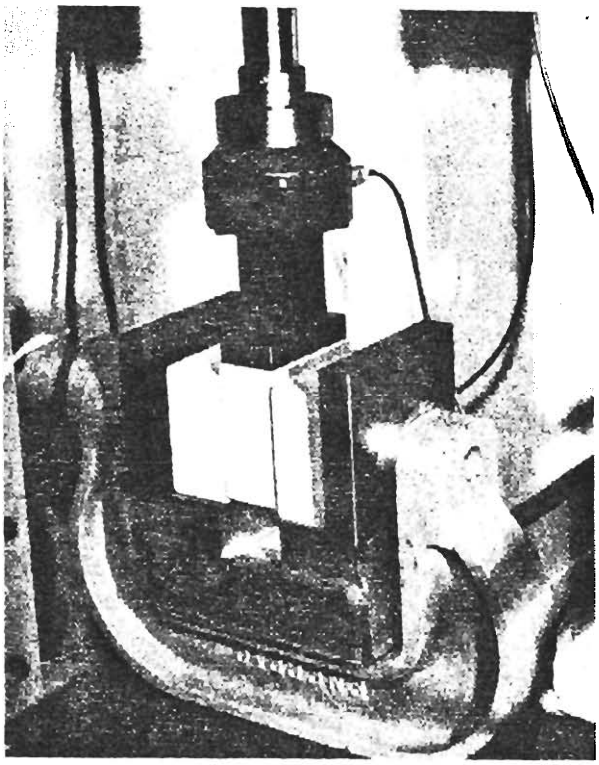

FIG. 14. Friction experiment setup.

Static-Friction Measurements

Static frictional curves in which applied frictional stress to initiate slip is plotted against normal stress for several surface finishes on Indiana limestone and Nugget sandstone have been previously presented.[11] It was found there that the presence of water decreased friction in the sandstone and increased friction in the limestone. More recently we have employed lubricants to further reduce the friction effects. Two lubricants found to be quite effective are HI-TEMP C-100, Anti-Ball Lubricant* and 630-AA Lubriplate.† A friction plot for Indiana limestone is presented in Fig. 15. It is seen that these lubricants significantly reduce the frictional load necessary to initiate slip below that for wet and dry surfaces. Similar reductions were found on Nugget sandstone surfaces. These data and extrapolations thereof are used to estimate the shear frictional stress that an interface can support when it is under a load in one of the hydraulic fracture experiments.

Hydraulic Fracture-Interface Experiments

The purpose of the hydraulic fracture-interface experiments is to gain an understanding of the parameters that determine whether or not a fluid-driven crack will cross an interface and penetrate the adjacent rock structure. This knowledge has application in the placement of hydraulic fracture for optimum reservoir stimulation. Among these parameters are the frictional properties of the interface and the presence of existing fractures near the interface. Some results from these interface experiments have been reported.[11] It was found that for the Indiana limestone and the Nugget sandstone these exists a critical threshold normal stress

*Manufactured by FEL-PRO, INC., Skokie, IL.
†Manufactured by Fiske Bros. Refining Co., Newark, NJ, and Toledo, OH.

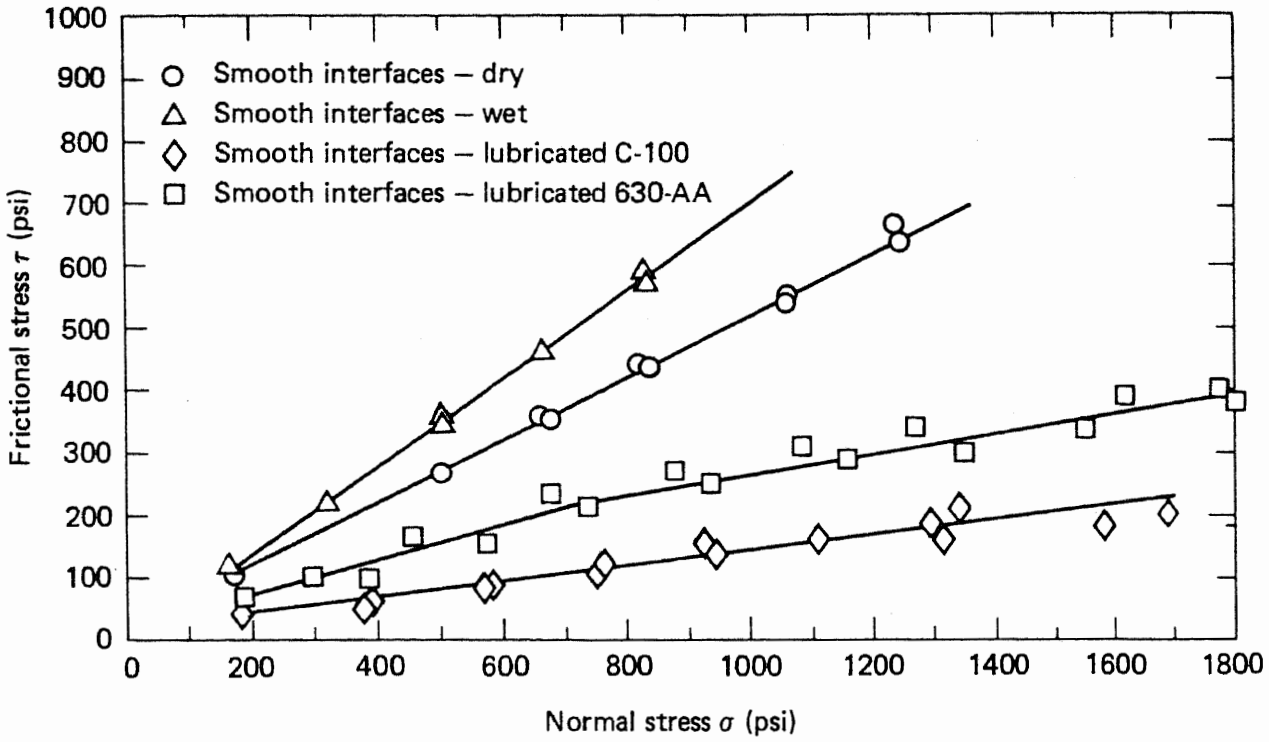

FIG. 15. Static friction plot for different surface conditions of Indiana limestone.

across the interface below which the crack will not penetrate the interface into the adjacent rock. These normal stress thresholds (normally 4.5 MPa and 5.5 MPa for the limestone and sandstone, respectively) were converted to threshold shear stresses from the friction curves such as in Fig. 15. More recent hydraulic fracture-interface experiments in which the lubricants were applied to the interface have been performed. As one would expect, the effect of the lubricant was to increase the threshold normal stress. The results from these experiments are summarized in Table 2. As can be seen from the table, the threshold frictional shear stress decreases

TABLE 2. Threshold stresses for crack growth across unbonded interfaces (MPa).

Material	Dry	Lubricated		
		Water	630-AA	C-100
Indiana limestone	4.5	3.4	9.7	15.2
	(2.4)	(2.4)	(2.3)	(2.0)
Nugget sandstone	5.5	6.5	—	11.7
	(2.8)	(2.6)	—	(2.0)

Note: Upper entry is normal stress.

Lower entry (in parenthesis) is shear stress from friction plots.

with increasing threshold normal stress as the interface frictional coefficient decreases due to lubrication. This decrease in the threshold shear stress that the interface must support could be due to the fact that a greater difference in principal stresses exists because of the increased applied normal load.

A change in the frictional properties of an interface, such as one region having a lower coefficient of friction than an adjacent region, can also influence crack propagation across the interface. Figure 16 shows the result of an experiment in which a 3/4-inch strip of the C-100 lubricant was coated on an otherwise smooth, dry limestone interface parallel to the fluid injection tube. The opposite interface contained no lubricant whatever. The three-block stack was placed in a press and a load in excess of the threshold for cracks to cross the interface was applied. As can be seen in the figure, at the interface with the lubricated strip the crack reached the interface within the strip and then continued into the adjacent block laterally displaced to the edge of the lubricated zone. At the interface containing no lubricant the crack continued directly across the interface. Analysis indicates that if a crack tip is approaching the neighborhood on an interface where the coefficient of friction suddenly increases, a concentration of shear stress will occur at the discontinuity. This shear stress concentration makes crack initiation across the interface more likely at the discontinuity than directly across the interface and this is what is qualitatively shown in Fig. 16. This experiment again demonstrates that frictional characteristics at the interface affect the geometry of fracture growth.

Calculations have been performed to assess the effects of existing cracks near an interface on the growth of a fluid-driven crack across that interface.[3] Using the Mode I stress intensity factor as a criterion for crack growth, the results showed that the presence of cracks on the opposite side of the interface from the approaching fluid-driven crack had the same effect as lowering the elastic modulus across the interface. Having the elastic modulus suddenly drop across the interface was shown to have the effect of drawing the fluid-driven crack to the interface but inhibiting the growth on the opposite side of the interface into the adjacent material. Experiments have been performed to simulate the geometry of these calculations. The standard

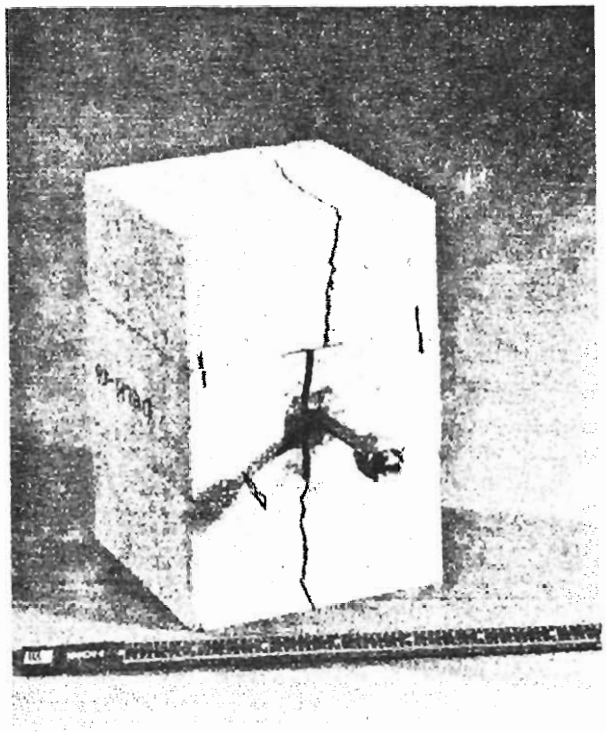

FIG. 16. Effect of a low friction region on crack growth across an unbonded, loaded interface.

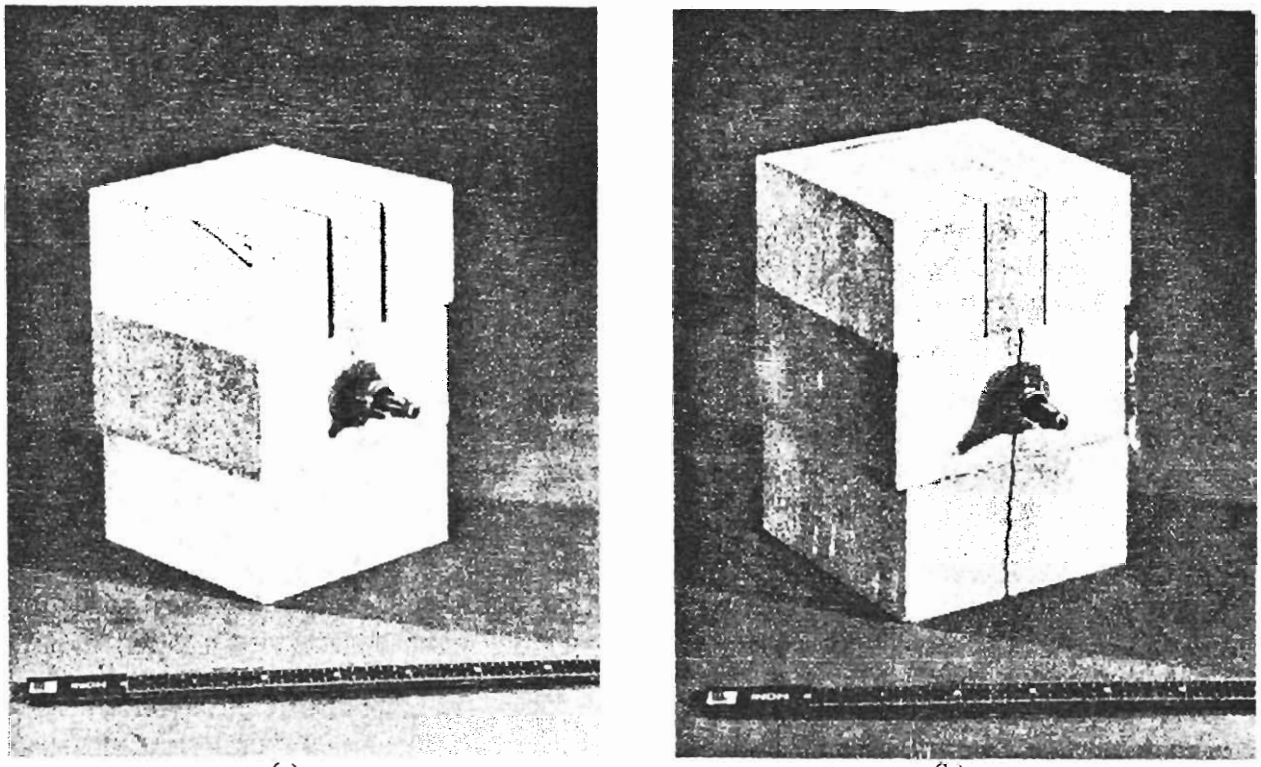

(a) (b)

FIG. 17. Effect of perpendicular cracks intersecting an interface on crack growth across the interface: (a) before fracturing, (b) after fracturing.

three-prismatic limestone block setup with two interfaces, one on each side of the injection tube, was used as shown in Fig. 17. However, one of the outer blocks was actually three smaller blocks sitting parallel to give the effect of two perpendicular cracks intersecting the interface as shown in Fig. 17a. The block assembly was then placed in a press and a load greater than the threshold load for crack penetration was applied. As seen in Fig. 17b, the crack crossed the lower interface into the solid block but terminated at the interface which was intersected by the existing cracks. Again this experiment qualitatively agrees with the prediction of the theoretical model.

EFFECT OF PRINCIPAL STRESS MAGNITUDE ON HYDRAULIC FRACTURE ORIENTATION

We carried out two sets of hydrofracturing tests in Dresser basalt designed to detect the effect of the principal stress magnitudes on fracture orientation. The emphasis was on the effect of borehole fluid viscosity on hydrofracturing results. To carry out these tests we used different hydraulic oils of known viscosities under a preset state of stress. Two conditions were investigated: (1) where the largest horizontal compressive stress (σ_H) was only slightly larger than the least horizontal stress (σ_h), and both were considerably smaller than the vertical stress (σ_V), and (2) where σ_V was substantially less than either σ_H or σ_h.

We observed no distinct difference in fracture direction, which is almost always guided by the direction of the least horizontal stress. Differences between viscosities were obtained in breakdown pressure magnitudes and in the acoustic emission during hydrofracturing. It seems that the higher the viscosity, the larger the breakdown pressure and the more prolonged the acoustic emission.

We originally intended to use Montello granite, which we had used extensively in previous tests with water as the borehole fluid. With this granite, it is relatively easy to prepare specimens and to detect hairline hydrofractures. Because this material was not available for the present tests, we used Dresser basalt,[12,13] also previously tested with water. Since Dresser basalt is more difficult to prepare and produces a high percentage

of rejects due to excessive preexisting fractures, costs were increased and results were less than consistent with respect to breakdown pressure magnitudes, which appear to be greatly affected by preexisting fractures. The objectives of the experiment, however, were fully accomplished.

Results

The experimental setup was described in a previous report.[13] We used three high-viscosity hydraulic oils ranging from 247 cSt to 1260 cSt (centistoke), and compared the results with those obtained in water (1 cSt). Borehole pressure was maintained by pumping the fluid at a constant rate. In all tests shown, the hydraulic line was shut-in as soon as pressure was steady. The results are detailed in Tables 3 and 4.

With water, the breakdown point was reached suddenly, without any warning in the pressure-time record, and the pressure chopped fast and uncontrollably after shut-in. Acoustic emission events significantly above the background noise began shortly before breakdown and continued for the brief duration of the pressure drop.

TABLE 3. Effect of horizontal stresses on hydrofracturing orientation and breakdown pressure in Dresser basalt for various fluid viscosities.

Specimen number	Viscosity, cSt	Least horizontal stress (σ_h), psi	Breakdown pressure, psi	Vertical hydrofracture orientation with respect to σ_h
404	1	1800	4800	45°
303	1	1800	5000	90°
203	1	1800	4500	75°
504	1	1850	4300	80°
402	1	1900	4450	70°
204	1	1950	3400	75°
401	1	1975	4100	90°
104	1	2000	5600	60°
104-095	247	1850	6200	55°
105-095	247	1900	7200	70°
110-095	247	1925	5400	irregular
106-095	247	1950	3050	90°[a]
108-095	247	1950	N.A.	80°
109-095	247	1950	N.A.	80°
121-240	627	1800	8000	irregular
112-240	627	1850	7250	80°[a]
114-240	627	1900	5880	85°
120-240	627	1925	8840	70°
115-240	627	1950	6930	80°
118-240	627	1950	8000	80°
119-240	627	1975	7350	80°
125-480	1260	1800	8040	70°
126-480	1260	1925	7800	60°
127-280	1260	1950	7840	70°
128-480	1260	1975	9800	80°

Note: Vertical stress, σ_V, = 4000 psi.
Largest horizontal stress, σ_H, = 2000 psi.

[a]Prefractured.

TABLE 4. Effect of vertical stress on hydrofracture orientation and breakdown pressure in Dresser basalt for various fluid viscosities.

Specimen number	Viscosity, cSt	Vertical stress (σ_V), psi	σ_h/σ_V	Breakdown pressure, psi	Hydrofracture attitude
3-1	1	500	4	4350	Vertical ⊥ to σ_h
2-2	1	750	8/3	3600	Horizontal
5-1	1	750	8/3	3650	Vertical ⊥ to σ_h
2-3	1	1000	2	5050	Vertical ⊥ to σ_h
111-095	247	500	4	6500	Vertical ⊥ to σ_h
113-095	247	1000	2	4210	Prefractured
124-240	627	500	4	6480	Vertical ⊥ to σ_h
123-240	627	750	8/3	5750	No visible fracture
122-240	627	1000	2	6990	Vertical ⊥ to σ_h
132-480	1260	500	4	8840	Vertical ⊥ to σ_h
131-480	1260	750	8/3	9050	Vertical ⊥ to σ_h
129-480	1260	1000	2	8500	Vertical ⊥ to σ_h

Note: Smallest horizontal stress, σ_h, = 2000 psi.
Largest horizontal stress, σ_H, = 4000 psi.

With oil, the breakdown point was reached slowly, with the pressure increase coming to a slow halt, followed by a slow, controllable drop after shut-in. Pressure leveled at a value slightly higher than the least compressive horizontal stress (σ_h), yielding the "shut-in pressure" value, and continued to go down only when the hydrofracture reached the outside face of the specimen. Some acoustic emission took place during the pressure drop. The higher the viscosity of the fluid the longer it took the pressure to drop after shut-in, and the acoustic emission was spread out more in time.

One interpretation of these results is that as fluid viscosity is increased, hydrofracture expansion slows and is easier to control. We were thus able to stop some fractures before they reached the outside face of the specimens.

Table 3 gives the preset state of stress in each specimen tested and the resulting breakdown pressure and hydrofracture direction for minor variations in σ_h. Within each group of viscosities there is some variation in the breakdown pressure owing to inhomogeneities and preexisting fractures in some of the specimens. However, it is quite clear from Table 3 that generally the breakdown pressure increases as the fluid viscosity is increased. All hydrofractures obtained were vertical and for the small differential stress ($\sigma_H - \sigma_h$) used 25–200 psi) it is surprising how close the fractures are to being perfectly perpendicular to σ_h direction.

Table 4 gives the results of tests in which the vertical stress, σ_V, was kept significantly lower than the smallest horizontal stress (σ_h). Almost invariably the resulting hydrofracture was vertical and perpendicular to σ_h irrespective of the viscosity of fracturing fluid. Again, the breakdown pressures increase with the viscosity.

GEOLOGY/GEOPHYSICS

FRACTURES AND STRUCTURAL GEOLOGY IN THE PICEANCE BASIN, NORTHWEST COLORADO

Following our general and theoretical work on fractures and their relation to gas production,[14] it seemed desirable to examine actual structural and fracture data in one of the western "tight gas-sand" basins. Work related to oil shale exploration and development in the Piceance Basin in northwestern Colorado provides a unique opportunity to compare geologic structure, surface fractures, and hydraulic fractures. The information covers about 1500 square miles (3900 square kilometers) of gently folded and faulted Green River Formation.

Natural surface fractures in the basin tend to be oriented parallel to fold axes, except on the plunging ends of folds, where they more nearly parallel the rock strike or the structural contours. As might be expected, surface fractures parallel surface tension faults where they are present.

Hydraulic fractures made in shallow holes tend to strike parallel to the natural surface fractures. Although the hydraulic fractures were made in sections of rock that appeared to be unfractured, they may have followed undetected incipient fractures or a related discontinuity or element of rock fabric. If they lie parallel to the direction of the maximum principal *in situ* stress, as intended, then the surface faulting and fractures were formed by stresses similarly oriented. The orientation of the surface structural features, then, might be used to predict the orientation of natural fractures and hydraulic fractures.

This should be tested by (a) detailed surface mapping of structure and fractures; (b) examination of oriented cores for macrofractures, microfractures, and other micro-fabrics; (c) *in situ* stress measurements at intervals from near the surface to potential reservoirs; (d) experimental hydraulic fractures at similar depths, with determination of the azimuths and dimensions of the resulting fractures. This would test the predictive use of surface and shallow information and would determine the congruence, if any, of shallow stresses and strain features with those at depth.

The structural information used here is from surface mapping and shallow boreholes in the Green River Formation.[15–17] The surface rocks are folded into a series of northwest-southeast folds with low dips, and structural elevations are lower toward the basin's axial syncline in the north and northeast part. Normal faulting is commonly mapped on and near anticlinal axes. These features do not correspond either to the generally east-west direction of Late Cretaceous-Early Paleocene regional compression or to the alternative hypothesis of a left-lateral nearly east-west couple. They are more readily explained by bending tension or by folding due to sag over deeper structures.

Welder's mapping of joint patterns from air photos[18] has the usual deficiencies of such data, but basin-wide mapping was accomplished. More detailed surface work would be desirable, together with additional information on joint attitude and surface features. As the mapping is almost entirely on the Evacuation Creek Member of the Green River Formation, variance due to lithologic type should not be an important factor in interpretation of the joint patterns. Frequency of jointing (measured as number of joints per township) varies as much as threefold, but no pattern or correlation can be seen. Variation is possibly simply due to degree of fresh bedrock exposure.

Map data were first compiled for each township, by counting the numbers of fractures mapped in each ten-degree segment of azimuth. These were reduced to percentages and then plotted in a rosette for each township. One or two strong concentrations of joint direction commonly occur; there is a strong tendency towards a northwest-southeast orientation. As has also been noted elsewhere, the joints have a tendency to parallel fold axes on the axis and flanks of folds but to be rotated closer to the strike directions around the plunging ends. The joints in the vicinity of faults strongly tend to parallel the faults.

Further analysis would require information on the joints' dip and surface features. The distribution pattern leads one to suspect that both tension and shear fractures are present.

Wolff[19] has made *in situ* stress measurements in a number of holes in the Green River Formation at depths ranging from 118 to 1564 ft (36 to 477 m). Sections of open hole without apparent fractures were selected after acoustic logging with a "borehole televiewer." These were then packed off and a small fracture

made by hydraulic pressure (a mini-fracture) and propped open. Post-fracturing televiewer logs enabled the operators to "see" the new fractures and to determine their direction at the borehole. That direction is considered to be normal to the direction of least principal stress. Fractures below 400 ft (122 m) were all dipping within 12 degrees of vertical. Shallower fractures were either not present or horizontal. Some fractures could not be seen, some pressures were confusing, some fractures could only be seen on one side of the hole, and of course only the apparent direction right at the borehole wall could be seen. Many useful data were obtained, however. Figures 18 and 19 show reported fracture directions and differentiate between the poor or questionable data and those that appear "good." There is a strong degree of parallelism between the mini-fractures and surface joints and faults. The parallelism may continue in depth, or the controlling stresses or the strain features from present and past stress systems may change. This needs to be determined by more data from deep holes.

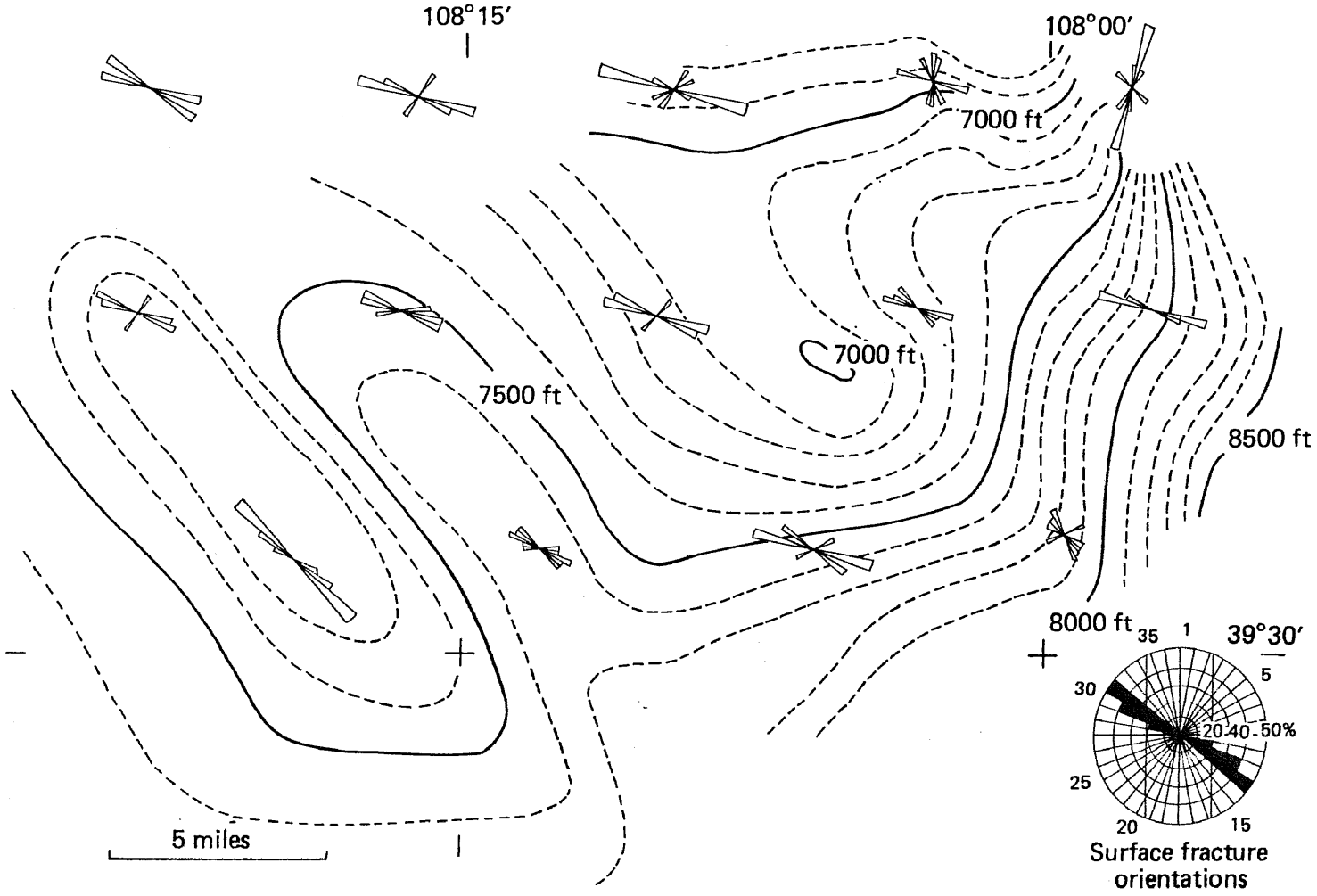

FIG. 18. Structure and surface fractures in the south part of the Piceance Basin, northwest Colorado. The rosettes depict surface fractures mapped from air photographs. Each ray is proportional to the percent of the total mapped in a township in 10° of arc. Values less than 10% are not plotted. Major fractures generally parallel fold axes along their flanks; on fold noses they turn toward the strike direction. Structure contours are on the Green River 'mahogany marker'. Elevations are in feet above sea level.

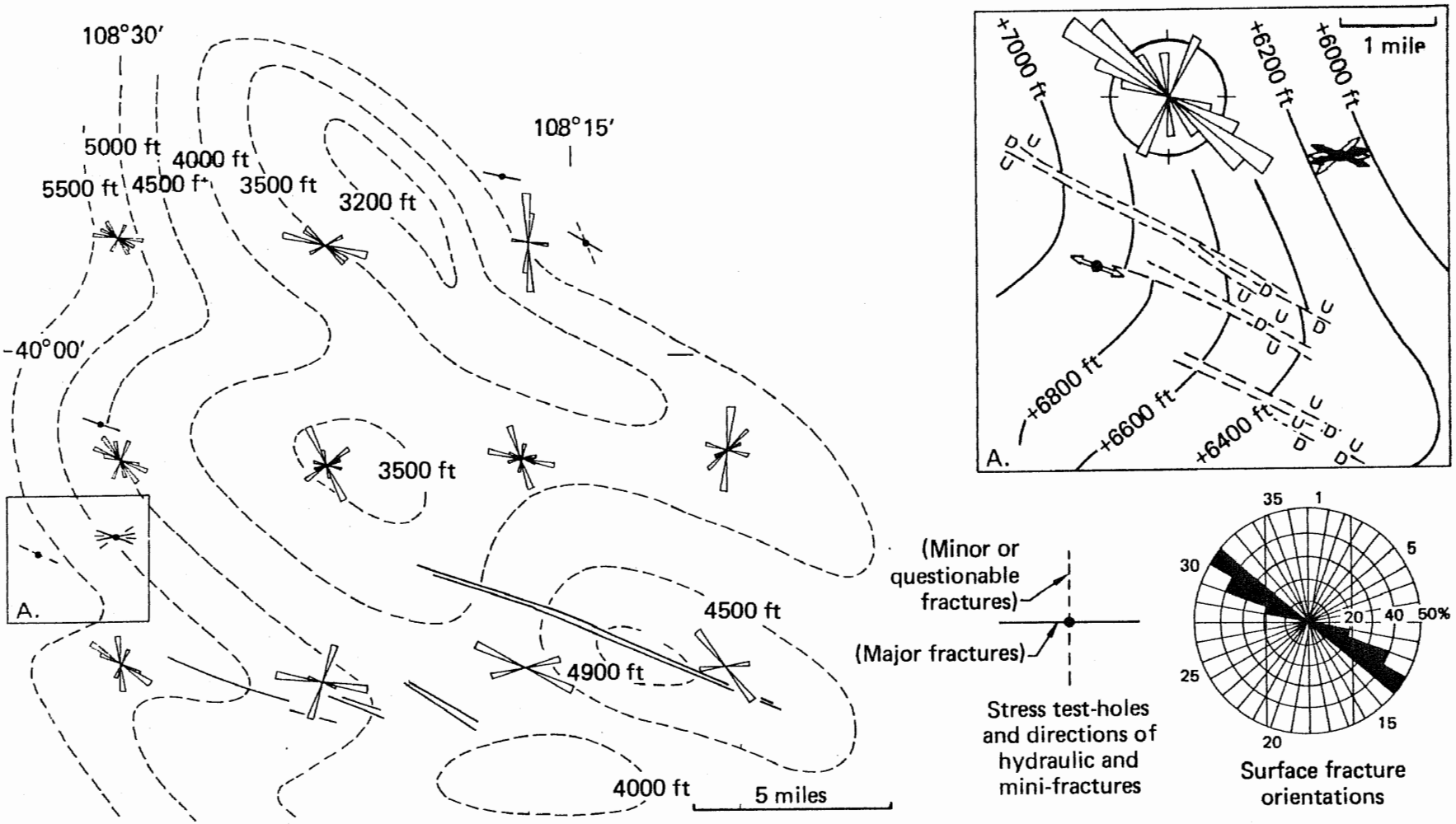

FIG. 19. Structure, surface fractures, and hydraulic fractures in the north part of the Piceance Basin, northwest Colorado. Major surface fractures tend to parallel the tension faults exposed on the surface. Mini-fractures produced in test holes to determine stress directions tend to form parallel to surface fractures and faults. Structure contours are on the Green River 'orange marker'. Elevations are in feet above sea level. The inset is a detailed map of area 'A', showing a diagram of surface joints and direction of major and minor mini-fractures in stress tests (arrows). Contours are on 'A groove'.

ROCK MECHANICS MEASUREMENTS

Current methods for predicting fracture intensity, geometry, and extent resulting from fracturing stimulation (using either high explosive or hydraulic means) of an initially impermeable natural gas bearing rock require certain equation-of-state (EOS) measurements as input data to the calculation codes. We continued to generate the required EOS data for Mesaverde sandstone (reservoir rock) and shale (source rock) core sections from the Twin Arrow well No. C&K 4-14 in Rio Blanco County, Colorado, and the Federal No. 24-19 well in Sublette County, Wyoming. The depth of sample origin ranged from 349.9 to 354.5 m for the Colorado well and 1579.9 to 1582.8 m for the Wyoming well.

The core sample contains alternating sections of sandstone, shale, and the mixture of the two. The sandstone sections are quite homogeneous. The bedding planes between sandstone and shale are horizontal (perpendicular to the axis of core sample). However, within the sections of pure sandstone or shale, the bedding is not obvious. For the Colorado rocks, the shale sections show different colors at different depths. At 349.9 m the shale is black-gray; at 351 m it becomes gray; at 354 m it contains bands of yellow-gray; at 358 m the shale is pure gray. For the Wyoming rocks, the colors of the sandstone and shale are light gray and dark gray, respectively. The sandstone is very fine grained.

To date, we have completed the pressure-volume measurement for the Mesaverde sandstone from Rio Blanco County, Colorado. The specimens were right cylinders of about 1.27 cm diameter and 2.54 cm long, cored either parallel or perpendicular to bedding. Volumetric strain as a function of confining pressure, up to a pressure of 1.2 GPa, was determined by strain measurements of longitudinal and radial strain gages. Typical data of pressure-volume measurements are shown in Figs. 20 and 21. These are the pressure-volume data of the first pressure cycle. Figure 20 shows the data of one specimen cored parallel to bedding; Figure 21 shows the data of another specimen cored perpendicular to bedding. Both figures show the nonlinear characteristic of a porous rock under hydrostatic compression.

We also completed the plumbing of the high pressure system for simultaneous ultrasonic velocity measurements in multiple directions up to a confining pressure of 1.0 GPa. The calibration and debugging of the system were started. These will be continued in the next quarter.

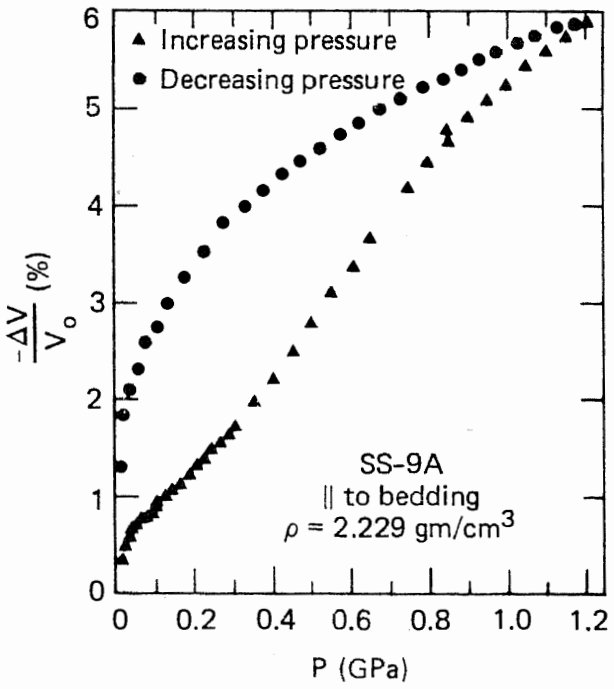

FIG. 20. Pressure-volume relationship for Mesa Verde sandstone from Rio Blanco County, Colorado, for specimen cored parallel to bedding.

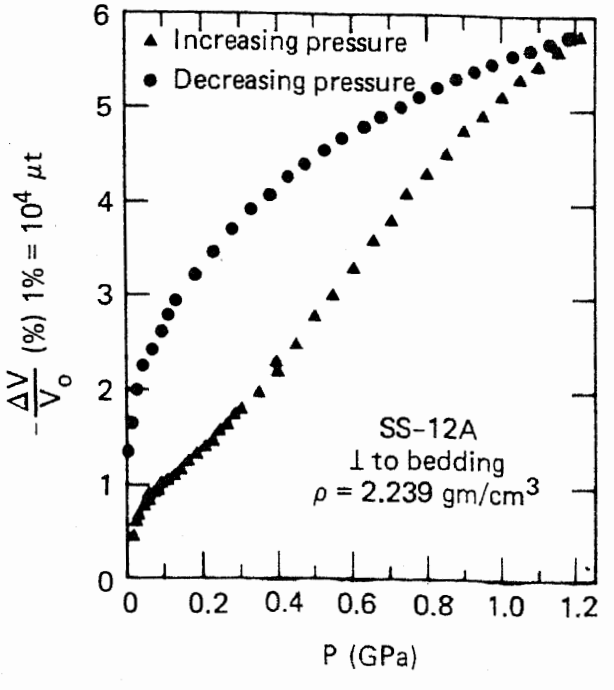

FIG. 21. Pressure-volume relationship for Mesa Verde sandstone from Rio Blanco County, Colorado, for specimen cored perpendicular to bedding.

REFERENCES

1. A. G. Petschek and M. E. Hanson, "Difference Equations for Two-Dimensional Elastic Flow," *J. Comp. Phys.* **3**, 307 (1968).
2. D. S. Kershaw, *The Incomplete Cholesky-Conjugate Gradient Method for the Iterative Solution of Systems of Linear Equations*, Lawrence Livermore National Laboratory, Livermore, CA, UCRL-78333, Rev. 1 (1977).
3. M. E. Hanson and R. J. Shaffer, *Some Results from Continuum Mechanics Analysis of the Hydraulic Fracture Process*, American Institute of Mining Engineers, Dallas, TX, SPE 7942 (1979).
4. R. J. Shaffer, M. E. Hanson, and G. D. Anderson, *Hydraulic Fracturing Near Interfaces*, Lawrence Livermore National Laboratory, Livermore, CA, UCRL-83419 (1979). Presented at ASME Energy & Technology Conf., New Orleans, Feb. 3, 1980.
5. K. Arin and F. Erdogan, "Penny-shaped Crack in an Elastic Layer Bonded to Dissimilar Half Spaces," *Int. J. Eng. Sci.* **9**, 213–232 (1971).
6. M. E. Hanson, G. D. Anderson, R. J. Shaffer, W. Lin, D. F. Towse, M. P. Cleary, and B. C. Haimson, *LLL Gas Stimulation Program Quarterly Progress Report, April through June 1979*, Lawrence Livermore National Laboratory, Livermore, CA, UCRL-50036-79-2 (1979).
7. M. E. Hanson, G. D. Anderson, R. J. Shaffer, D. F. Towse, W. Lin, L. D. Thorson, and M. P. Cleary, *LLL Gas Stimulation Program Quarterly Progress Report, October through December 1979*, Lawrence Livermore National Laboratory, Livermore, CA, UCRL-50036-79-4 (1979).
8. M. E. Hanson, G. D. Anderson, R. J. Shaffer, D. F. Towse, J. R. Hearst, W. Lin, and M. P. Cleary, *LLL Gas Stimulation Program Quarterly Progress Report, July through September 1979*, Lawrence Livermore National Laboratory, Livermore, CA, UCRL-50036-79-3 (1979).
9. J. Geertsma and F. deKlark, "A Rapid Method of Predicting Width and Extent of Hydraulically-Induced Fractures," *J. Pet. Tech.* **1471**, (1969).
10. G. C. Howard and C. R. Fast, *Hydraulic Fracture*, Society of Petroleum Engineers Monograph (1970).
11. G. D. Anderson, *The Effects of Mechanical and Frictional Rock Properties on Hydraulic Fracture Growth Near Unbonded Interfaces*, American Institute of Mining Engineers, Dallas, TX, SPE 8347 (1979).
12. M. E. Hanson, G. D. Anderson, R. J. Shaffer, D. N. Montan, B. Haimson, and M. P. Cleary, *LLL Gas Stimulation Program Quarterly Progress Report, January through March 1978*, Lawrence Livermore National Laboratory, Livermore, CA, UCRL-50036-78-1 (1978).
13. M. E. Hanson, R. J. Shaffer, G. D. Anderson, D. N. Montan, W. Lin, B. Haimson, and M. P. Cleary, *LLL Gas Stimulation Program Quarterly Progress Report, October through December 1977*, Lawrence Livermore National Laboratory, Livermore, CA, UCRL-50036-77-4 (1978).
14. D. Towse, *A Review of the Mechanics and Occurrence of Natural Fractures in Rock as Applied to the Development of the Tight Western Gas Sands*, Lawrence Livermore National Laboratory, Livermore, CA, UCRL-52908 (1980).
15. J. R. Donnell, *Tertiary Geology and Oil-Shale Resources of the Piceance Creek Basin Between the Colorado and White Rivers, Northwestern Colorado*, U.S. Geological Survey Bulletin 1082-L (1961).
16. J. R. Dyni, "Structure of the Green River Formation, Northern Part of the Piceance Creek Basin, Colorado," *The Mountain Geologist* **6**, 57–66 (1969).
17. E. A. Ziemba, "Oil Shale Geology, Federal Tract C-a, Rio Blanco County, Colorado," in *Energy Resources of the Piceance Creek Basin, Colorado* (Rocky Mountain Association of Geologists, Denver, CO, 1974), pp. 123–130.
18. F. A. Welder, Map Showing Joint Pattern Inferred from Aerial Photographs (unpublished map—1970).
19. R. G. Wolff, J. D. Bredehoeft, W. Scott Keys, and E. Shuter, "Tectonic Stress Determinations, Northern Piceance Creek Basin, Colorado," in *Energy Resources of the Piceance Creek Basin, Colorado*, (Rocky Mountain Association of Geologists, Denver, CO, 1974), pp. 193–197.

SB/ks/prl